Multiscale Electro-Chemo-Mechanics Interaction and Degradation Analytics of Sn Electrodes for Sodium-ion Batteries

Susmita Sarkar¹, Hernando J. Gonzalez-Malabet², Megan Flannagin², Alex L'Antigua², Pavel D. Shevchenko³, and George J. Nelson^{2,*}, and Partha P. Mukherjee^{1,*}

*Correspondence: george.nelson@uah.edu (G. J. Nelson); pmukherjee@purdue.edu (P. P. Mukherjee)

¹School of Mechanical Engineering, Purdue University, West Lafayette, Indiana 47907, United States ²Department of Mechanical and Aerospace Engineering, The University of Alabama in Huntsville, Huntsville, Alabama 35899, United States

³Advanced Photon Source, Argonne National Laboratory, Lemont, Illinois 60439, United States

ABSTRACT

Sodium-ion batteries (SIB) have emerged as a strong contender among the beyond lithium-ion chemistries due to elemental abundance and the low cost of sodium. Tin (Sn) is a promising alloying electrode with high capacity, redox reversibility, and earth abundance. Tin electrodes, however, undergo a series of intermediate reactions exhibiting multiple voltage plateaus upon sodiation/desodiation. Phase transformations related to incomplete sodiation in tin during cycling, in the presence of a frail solid electrolyte interphase (SEI) layer, can quickly weaken the structural stability. The structural dynamics and reactivity of the electrode/electrolyte interface, being further dependent on the size and morphology of the active material particle in the presence of different electrolytes, dictates the electrode degradation and survivability during cycling. In this study, we paint a comprehensive picture of the underpinnings of the electrochemical and mechanics coupling and electrode/electrolyte interfacial interactions in alloying Sn electrodes. We elicit the fundamental role of electrode/electrolyte complexations in the Sn electrode structure-property-performance relationship based on multi-modal analytics, including electrochemical, microscopy, and tomography analyses.

KEYWORDS

Tin anode • Sodium-ion batteries • X-ray microtomography • Carbonate electrolyte • Micro-nano particle

1. INTRODUCTION

With the upsurge of renewable energies, the demand for energy storage devices is contemporaneously escalating. As the search for a low cost, high yield, extended cycle-life, and reliable battery system for the resilient grid of the future gains momentum, the current infrastructure is languishing because of the high cost, low availability, and limited sustainability of critical materials. On the other hand, sodium (Na), one of the most earth-abundant and cost-effective alkali metals from the earth's crust (or ocean), shows enormous potential due to its excellent power and energy densities. The striking similarity with the state-of-the-art lithium-ion battery (LIB) technology also significantly decreases the lead time in the selection of electrode and electrolyte materials for Na-ion batteries.^{1–4}

Despite the configurational and operational resemblance with its Li-ion counterpart, the choice of electrode/electrolyte pair for Na-ion batteries is not mere serendipity.⁵ The electrode materials for SIBs exhibit different behavior and performance compared to LIB anodes.^{6–9} For example, the commonly used graphite (insertion-based) and silicon (alloy-based) anodes of LIBs are ineffective and demonstrate limited capacity in SIBs. Hard carbons are effective at reversible sodium insertion, but their capacity is also limited, and therefore the use of a different type of carbon nanostructured electrodes has been addressed to solve this issue.^{6,10–12}

Tin (Sn), a member of the alloy family, surprisingly demonstrates a high capacity for both Liion and Na-ion systems. However, additional challenges emerge, such as slower reaction kinetics, slower diffusion for Na in Sn, and drastic volumetric expansion induced by sodiation (>400%). Similar microstructural changes seen in Sn-based anodes for LIBs are also observable for SIBs. In addition to the disadvantages of the electrode material, unfortunately, the Na and Sn electrodes are

also subjected to the limitations from electrode-electrolyte interfacial reactions forming an unstable, fragile solid electrolyte interphase (SEI) layer in the presence of a liquid electrolyte.

An SEI layer should ideally form at the beginning of battery life and act as a passive layer while preventing continuous reaction and electrolyte decomposition during cell operation. An incompatible liquid electrolyte will create a soluble SEI. Such an SEI depletes the Na inventory and can lead to the dendrite formation. The failure mode of the SEI layer varies dramatically depending on the type of electrolyte and electrode used. Understanding the different degradation mechanisms of the electrode/electrolyte interface is essential to developing strategies for high-performance SIBs.¹³ The performances of SIBs with electrolytes can be improved through minor variations in composition such as electrolyte molar content or electrolyte additives or by adjusting the amount of solvent used to boost the system conduction of both cations and anions.¹⁴

Two of the most widely used SIB electrolytes are sodium hexafluorophosphate (NaPF₆) and sodium perchlorate (NaClO₄), diluted either in the organic solvents ethylene carbonate (EC), fluoroethylene carbonate (FEC), diethyl carbonate (DC), propylene carbonate (PC), or a mixed ratio of these solvents. Comparisons between the behavior of lithiated and sodiated Sn electrodes have been made with PF₆ and ClO₄ electrolytes. As research progressed, the adoption of FEC as a component within the solvent solution became more widespread. This addition proved to have a substantial impact and the stability of the SEI in all the commercially available binders such as polyvinylidene difluoride (PVDF), carboxymethyl cellulose (CMC), and polyacrylic acid (PAA). For PVDF-based electrodes, FEC addition increases the reversible ionic insertion and thus improves the long-term cyclability. ^{15–17} Although certain claims of comparable durable performance can be made without FEC, given optimal electrode formulation and preparation, FEC does serve to stabilize the SEI regardless. The relative instability of the SEI formed within PVDF-

based SIBs in comparison to their CMC counterparts makes the addition of FEC have a more substantial impact on the long-term performance of PVDF-based SIBs.¹⁶

Nevertheless, despite the significant effort in improving electrode material in different types of electrochemical conditions, the multiscale effect of intermediate reaction products and SEI formulation is yet unrecognized. This work aims to show the influence of both particle sizes and electrolyte mixtures on the electrochemical signatures of the Sn anode for SIBs. It is essential to recognize that the nonuniform surface structures hamper ionic mobilities and continuously modify the electrochemically active area, giving rise to anomalous electrochemical behavior. This study investigates the interaction between different electrolyte salt anions (ClO₄-, PF₆-) and electrolyte solvents. The interaction between these electrolyte components affects the micro/nano-structural evolution of the electrode, evident from the formation of several metastable phases and different reaction pathways. This fundamental study provides a mechanistic understanding of the correlation between electrolyte consumption and the multiscale structural evolution in Sn anodes caused by the different phase transitions that occur during cell operation.

2. EXPERIMENTAL SECTION

2.1.Electrode Fabrication and cell assembly

Sn electrodes were prepared using two distinct types of powder particle sizes, microparticles (MP) and nanoparticles (NP), using the "slurry casting" technique on a copper foil as the current collector. The powders were combined using a weight ratio of 70% Sn active material (AM), 19% carbon black (CB), and 11% PVDF, all diluted in 70% deionized water and 30% ethanol volume/volume. The casted electrode was left to dry overnight and then heated in a furnace under

vacuum at 80 °C for 10 hours, to remove the remaining moisture before battery assembly. The thickness of the electrode after drying is around 15 μ m.

Half-cell batteries were assembled in coin cell formats. Coin cell batteries were assembled in an argon-filled glove box with low O₂ and moisture content. The main working electrode was either a micro (10 μm) or nano Sn (<100 nm) electrode, which was paired with pure metallic Na as the counter electrode. A glass microfiber separator (GF/C, thickness 260 μm) was used between the working and counter/reference electrode. Two different types of electrolytes were prepared based on two salts, NaClO₄ and NaPF₆, both dissolved in 1M of propylene carbonate (PC) and PC-fluoroethylene carbonate (FEC). Sodium salts were vacuumed until dried before use.

2.2.Electrochemical Characterization

After cell fabrication, electrochemical characterization was done on the assembled batteries. Galvanostatic cycling with potential limitation (GCPL) was performed starting with five cycles of C/10 followed up with fifteen cycles of C/5, done in a voltage window from 0.0001V-0.8V. Cycled cells were then disassembled in an argon-filled box. During disassembly the Sn electrodes were cleaned using a PC solution.

2.3. Microstructural Characterization

2.3.1. XPS

X-ray photoelectron spectroscopy (XPS) was performed by the detector (Kratos ultra delay-line) connected to the argon gas glove box (the content of oxygen and water < 0.1 ppm), inside which the cells could be dissembled without air exposure.

2.3.2. XRD

X-ray diffraction (XRD) was done on pristine and cycled electrodes by applying Cu-K α radiation using a Rigaku MiniFlex 600 XRD system. Cycled electrode samples were handled in a glove box under an argon atmosphere and sealed in an air-tight sample holder for XRD measurements.

2.3.3. SEM

Scanning electron microscopy (SEM) imaging was obtained of the pristine and cycled electrodes using FEI NOVA nanoSEM Field Emission SEM.

2.3.4. X-ray Imaging

After cycling, the half-cells were disassembled in a controlled atmosphere glovebox. Samples were cut from the pristine and cycled Sn electrodes and sealed between two pieces of Kapton tape. Data from the pristine samples were analyzed to obtain a representative region of interest (ROI), where AM and supporting phases (CB and PVDF) could be easily differentiated.

Synchrotron-based X-ray microtomography (μCT) was performed on samples extracted from the composite electrodes at a resolution of 1.3 μm (0.65 μm pixel size) using beamline 2-BM at the Argonne National Laboratory Advanced Photon Source (APS). The μCT scans were performed in pink beam mode with an exposure time of 50 ms per projection image. Each tomographic scan contained 1500 projection images equally spaced over 180° of rotation. Samples for imaging were cut from bulk electrode samples using a 3 mm punch. Disks punched from the electrodes were encapsulated in Kapton tape and stacked to enable imaging multiple electrode samples at once. This approach follows the methods of Rajendra et al. and preserves contrast between the supporting carbon/binder regions, the open macropore phase, and the active material. In total, samples from six electrodes were examined, with representative regions from two electrodes

examined in detail. These samples corresponded to pristine and cycled electrodes of MP-Sn based active materials.

3. RESULTS AND DISCUSSION

Electrochemical Characterization

The electrochemical performance was studied for the different combinations of electrolyte blends and micro/nano Sn particles at a C/10 rate with a voltage range of 0.8V to 0.001 V vs. Na/Na⁺. Electrochemical performance signatures of Sn microparticles (MP) and nanoparticles (NP) for NaPF₆ and NaClO₄ based electrolytes with and without FEC are presented in **Figure 1**. The comparison between the Sn MP and NP shows that the nano-sized Sn has better capacity retention than those of micro-sized particles. After 10 cycles, the Sn MP possesses about 18.54% and 13.62% of capacity for ClO₄⁻:PC and PF₆⁻:PC. However, Sn NP exhibits increased (20.32% and 25.62% for ClO₄⁻:PC and PF₆⁻:PC, respectively) capacity for the same electrolyte. This enhancement in capacity retention of Sn nanoparticles, even without any special electrolyte additives, is primarily due to the reduced tendency for particle cracking and fewer detrimental effecta during cycling.

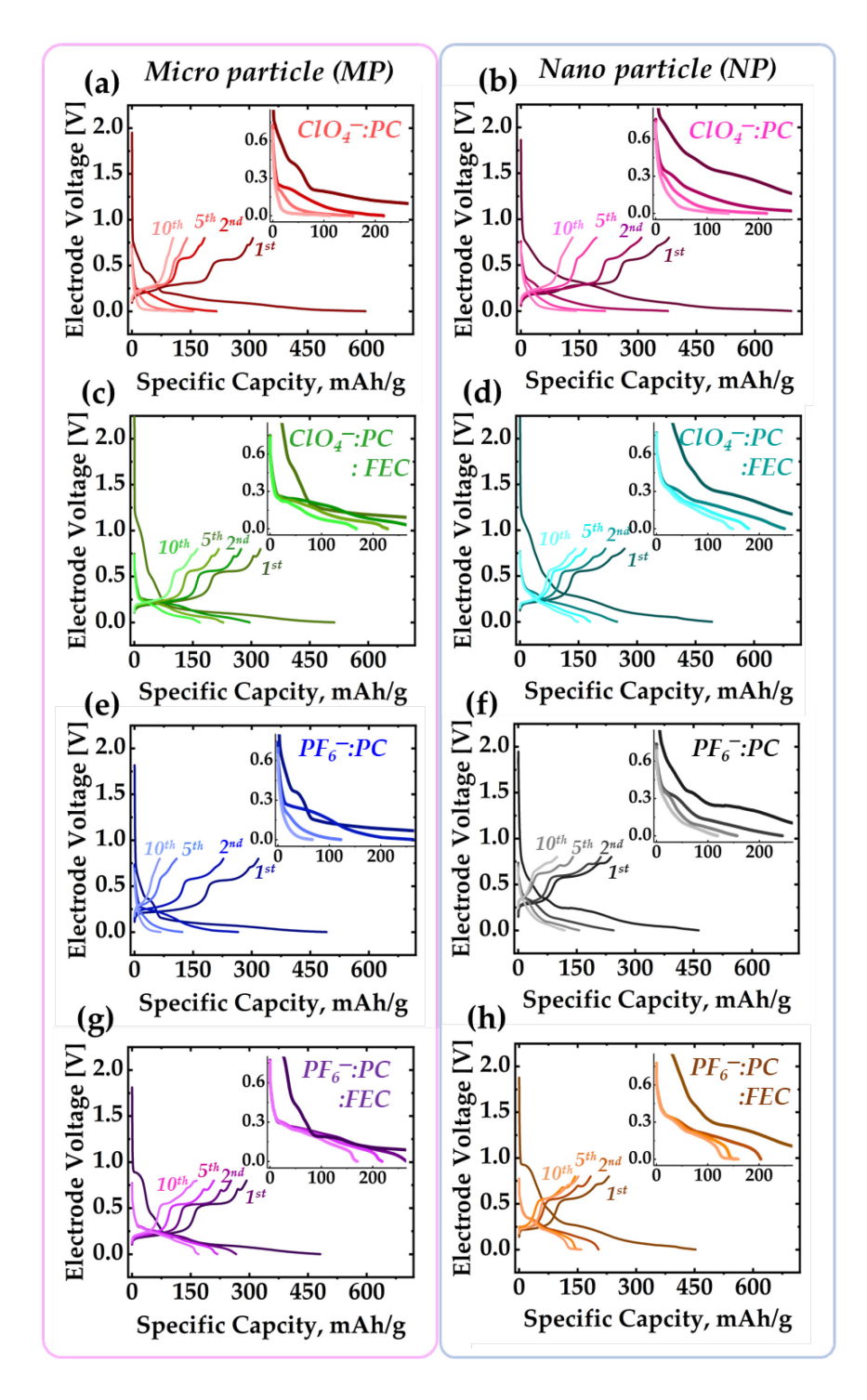


Figure 1. The charge-discharge curve of Sn microparticle (MP) and nanoparticle (NP) in different electrolytes: (a) MP: ClO₄⁻: PC, (b) NP: ClO₄⁻: PC, (c) MP: ClO₄⁻ PC: FEC, (d) NP: ClO₄⁻ PC: FEC, (e) MP: PF₆⁻: PC, (f) NP: PF₆⁻: PC, (g) MP: PF₆⁻: PC: FEC, and (h) NP: PF₆⁻: PC: FEC. The cells are cycled at 0.1 c-rate. The insets of the figure represent the zoomed-in discharge plots. It can be noted that the gap between the 1st and 2nd discharge curves for NP is always higher than the MP. This indicates that the change in charge transfer and SEI resistance is larger in NP.

Adding FEC improves the performance for both micro (ClO₄⁻-32.65%, PF₆⁻-35.29%) and nanoparticles (ClO₄⁻-30.19%, PF₆⁻-35.19%) with similar capacity retention. This indicates a more stable SEI formation with FEC, which tends to reduce the deleterious effect of alloying-induced mechanical interaction. Also, it is important to recognize that Sn MP and NP have similar performance on FEC-based electrolytes indicating that the effect of FEC is stronger than the positive effects of smaller particle size with a larger surface area. Moreover, larger charge-discharge hysteresis in Sn MP is observed than in the NP, indicating kinetic limitation and higher asymmetry in the sodiation and desodiation pathways for the MP.¹⁹

A deeper analysis of the voltage signatures can give us insights into the underlying dynamics of each electrode type. In general, the Sn MP electrode exhibits most of the capacity in the long plateau after 0.2 V. In contrast, Sn NP has monotonically decreased pseudo-plateaus, indicating continuously ongoing phase transformations. The decrease in discharge plateaus was also observed earlier with a decrement in particle sizes and can be attributed to the combined effect of microstructure (via a reduced ionic transfer path), crystalline structure (Increased bond length in the crystal structure causes weak atomic interactions), and electronic structure levels (Increased site energy due to larger surface area causes a decrease in the energy difference before and after ionic insertion).²⁰ Also, it can be noted that the gap between the 1st and 2nd discharge voltage is higher for NP than MP, indicating that more energy is lost during 1st discharge for NP. 21 The effect of electrolytes is quite pronounced. For ClO₄⁻ based electrolyte (without FEC), the electrochemical signature for the first cycle exhibits an initial linear potential decay until 0.45 V, followed by a second decay until 0.21 V and a long monotonically decreasing pseudo plateau till the end of discharge. For the NaPF₆ based electrolyte (without FEC), in addition to the initial linear potential decay, a flat region was detected around 0.19 V. When FEC is added, the linear potential

decay upon the first reduction gets prolongated, and a reduction in pseudo-plateau can be seen at 0.2 V vs. Na/Na⁺.

during charge/discharge Overvoltage generated is a good indicator the reversibility/irreversibility of a system. The larger the overvoltage, the sooner it will hit the charge/discharge-cutoff voltage, limiting the capacity by reducing the amount of inserted/extracted Na.²² Thus, understanding overvoltage-driven phase-state hysteresis is particularly useful in assessing the reversible capacity and change in reaction pathways for different particle sizes and electrolyte combinations. During the first charge cycle, the overvoltage is highest for PF₆-:PC (0.1106 V for MP and 0.1475 V for NP) while lowest for ClO₄⁻:PC (0.0923 V for MP and 0.0558 for NP). The addition of FEC helped to reduce the overvoltage for the PF₆⁻ case (0.1038 V for MP and 0.1398 V for NP), but this addition did not help for ClO₄⁻ (0.1069 V for MP and 0.1243 V for NP).

During the first cycle, where SEI is generally formed, Sn NP typically presents a larger overvoltage than that of MP. The ionic transport across the thicker SEI forming in the NP with a higher surface area and ionic polarization in the electrolyte is the main contributor to the overvoltage variation. After 10 cycles, the highest overvoltage is observed for NP with PF₆⁻:PC, signifying the difficulty of charge transfer in the unstable, thicker SEI layer. After cycling, the addition of FEC helped to reduce the overvoltage in all the cases, indicating the higher stability of the anode interface compared to the FEC-free case. This is also evident from the cycle life comparison that FEC-based electrolytes had the highest capacity retention for both MP and NP.

Coulombic efficiency is also another indicator of electrolyte stability. The Coulombic efficiency (CE) after the 1st cycle and 10th cycle for Sn MPs and NPs are shown in **Figure 2**. A strong correlation between particle size and the 1st cycle CE is evident. The higher surface area of

NP causes a more active SEI formation reaction at the electrode interface and consumes more Na ions from the inventory, leading to high irreversible capacity in the first cycle.²³ After 10 cycles, CE is more than 90% for all the cases (MP and NP) except for NP with the NaPF₆: PC. This electrolyte chemistry is unable to minimize the degradation in NP, where volume changes are still occurring at the nanoscale, causing unstable SEI at a larger surface area. Although MP might undergo severe volume change induced stress during cell operation, larger particles (MP) with a low surface area would be beneficial from a CE point of view.

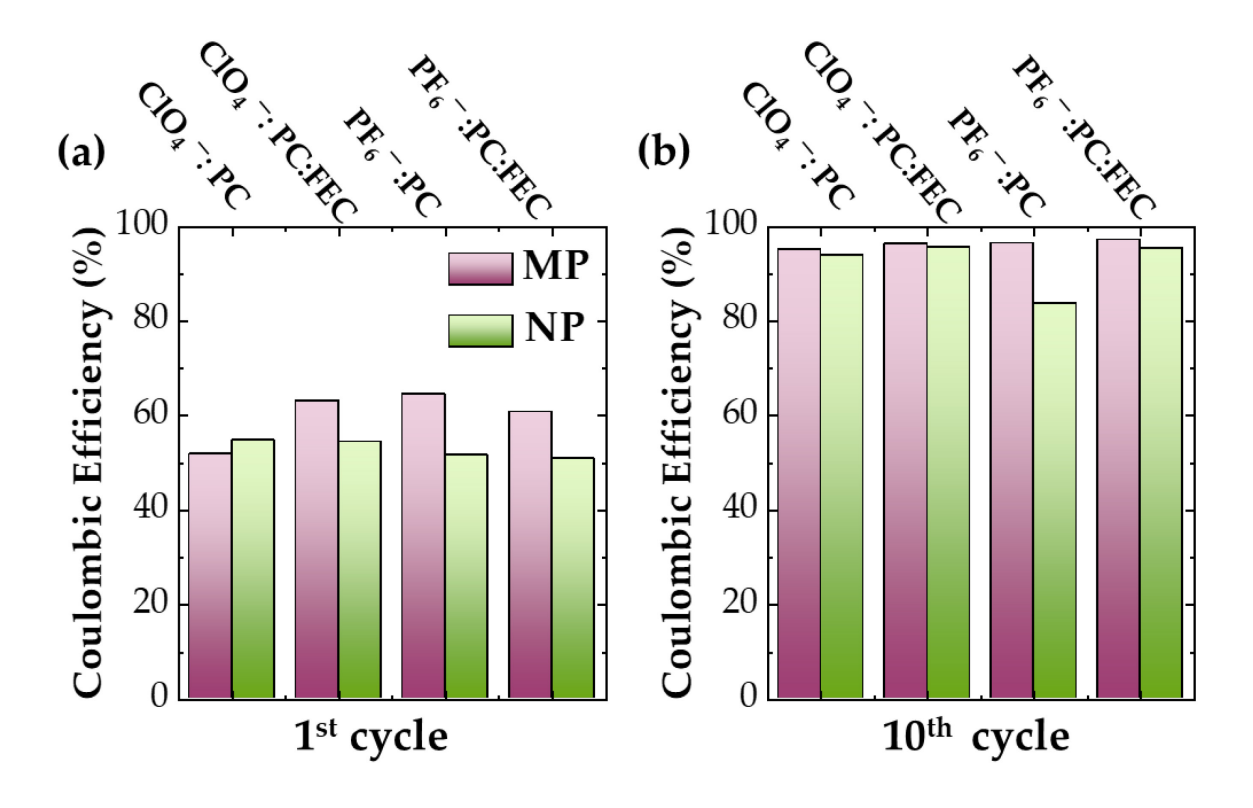


Figure 2. Coulombic efficiency of MP and NP Sn particle in different electrolytes: ClO₄⁻: PC, ClO₄⁻: PC: FEC, PF₆⁻: PC, and PF₆⁻: PC: FEC (a) after 1st cycle and (b) after the 10th cycle. The cells are cycled at 0.1 c-rate. Both MP and NP show low first cycle columbic efficiency, indicating the limitation of the electrolyte chemistry.

To reveal the nature of the Sn micro and nano particles-based electrode interface for different electrolyte environments, we have performed cyclic voltammetry (CV) with a low scan rate of

0.05 mV/sec to remove the kinetic limitations (Figure 3). In the literature, primarily two cathodic peaks were reported: 0.68 V corresponding to the formation of NaSn₃ and 0.26 V corresponding to Na₉Sn₄. ²⁴⁻²⁶ For our cases, multiple peaks were present during sodiation, indicating the presence of different intermediate phases. The position of the peaks varied depending on the type of the electrolyte and the size of the Sn particle. The first reductive peak, which shows a hint of SEI formation, appears at ~0.8 V for the MP: ClO₄⁻:PC. The addition of FEC shows a slightly earlier reductive peak, starting at 1.0 V (vs. Na/Na⁺) for both PF₆⁻ and ClO₄⁻. The electrolyte additive/ co-solvent has prior electrochemical reduction compared to the primary solvent, which leads to the formation of an effective SEI layer. The MP: PF₆⁻:PC also shows the 1st peak around 1.0 V, which is related to the formation of NaF in the presence of H₂O and HF. Nano-sized Sn also exhibits a similar pattern, where the ClO₄⁻:PC sample shows a late reductive peak around 0.5V, whereas the other cases show a peak around 1.0 V. Nanoparticle Sn with ClO₄⁻:PC shows a negative shift in reduction potential compared to the Sn MP. Three prominent anodic peaks were observed around 0.3 V, 0.6 V, and 0.7 V for MP:ClO₄⁻:PC, NP:ClO₄⁻:PC: FEC, NP:PF₆⁻:PC, and NP:PF₆⁻:PC: FEC. The addition of FEC with MP electrodes causes a peak at 0.3 V to be shifted at a slightly lower voltage indicating the formation of intermediate metastable phases. For MP:PF₆:PC, the peak at 0.6 V was missing. Instead, another peak at 0.77 V was observed. For NP:ClO₄:PC, an additional peak was observed at 0.177 V. In addition to that, peak broadening, especially in the first desodiation peak, can be seen for all the FEC free samples, which indicates the increase of overall cell resistance. This observation is consistent with overvoltage observations discussed earlier.

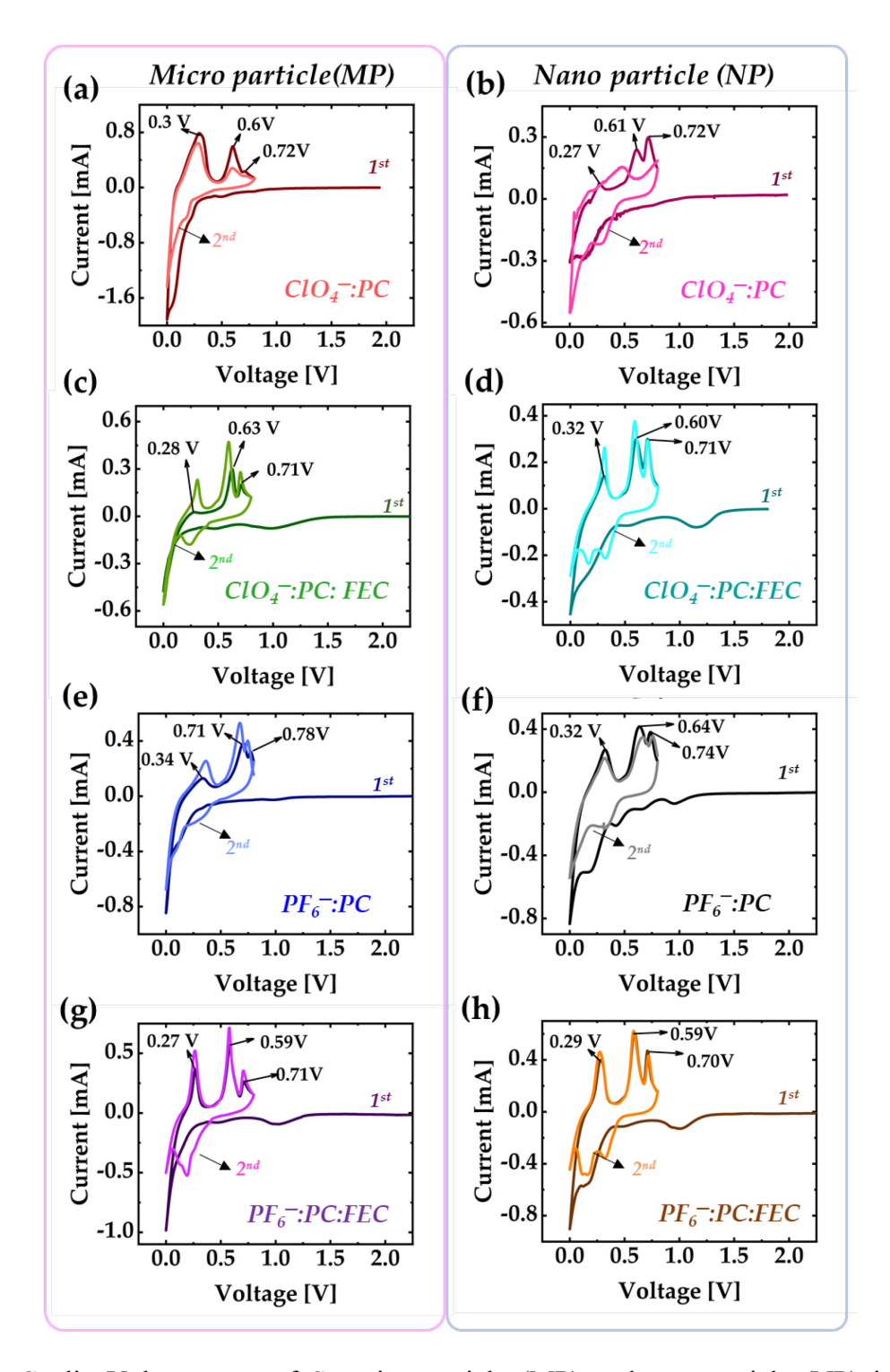


Figure 3. Cyclic Voltammetry of Sn microparticle (MP) and nanoparticle (NP) in different electrolytes: (a) MP: ClO₄⁻: PC, (b) NP: ClO₄⁻: PC, (c) MP: ClO₄⁻ PC: FEC, (d) NP: ClO₄⁻ PC: FEC, (e) MP: PF₆⁻: PC, (f) NP: PF₆⁻: PC, (g) MP: PF₆⁻: PC: FEC, and (h) NP: PF₆⁻: PC: FEC.. The cells are cycled at a scan rate of 0.05 mV/S. NP particles in the presence of PC only solvent, regardless of salt, show very weak peaks, indicating the formation of a less electrochemical active area.

The detailed analysis of the CV profile can be linked to the microstructural changes detected in each electrode with cycling. It can be observed that, for some combinations, the magnitude of the oxidation and reduction peaks increases with the number of cycles, which can be attributed to the continuous increase of the amount of electrochemically active Sn in each cycle. For example, the formation of micropores and exposure of surface area on fracture for MP:ClO₄⁻:PC: FEC, MP:PF₆⁻:PC, and MP:PF₆⁻:PC: FEC might be the reason for increasing peaks with cycling. SEI layer breakage for NP:ClO₄⁻:PC and formation of new electroactive particles for NP:ClO₄⁻:PC: FEC might be the possible cause for the enhancement in cathodic and anodic current density. On the other hand, for NP: ClO₄⁻:PC and NP: PF₆⁻:PC, the formation of a passivation layer on the surface of the electrode causes the magnitude of the oxidation and reduction peaks to decrease, indicating less electroactive area. For nanoparticles, due to the large surface area, a stronger signal should be detected; however, NP: ClO₄⁻:PC and NP: PF₆⁻:PC have weaker peaks, confirming the passivation layer formation. An in-depth discussion about the microstructural changes is in the following sections. Among ClO₄⁻ and PF₆⁻, the latter one has higher basicity which causes faster film growth. Thus, NP: PF₆⁻:PC has several unresolved tiny reductive waves in the 1 V – 0.4 V region.

Surface Elements Analysis using X-ray photoelectron spectroscopy (XPS)

To have a better grasp of the impact of the various electrolyte cocktails on the surface chemistry of the MP-Sn electrode after ten cycles, ex situ XPS measurements were carried out. The evolution of the SEI composition as a function of electrolyte composition is presented in Figure 4(a). Compared to the MP:ClO₄⁻:PC electrolyte, the fluorine content considerably increased for all the other cases with NaPF₆ salt or FEC solvent. The carbon content for MP:ClO₄⁻:PC: FEC and the oxygen content for MP:ClO₄⁻:PC are significantly higher.

The fitted spectrum for carbon (C), oxygen (O), and fluorine (F) is shown in Figure 4(b). The five C 1s peaks observed for MP:ClO₄⁻:PC, MP:PF₆⁻:PC, and MP:PF₆⁻:PC: FEC are representative of different carbon bonds corresponding to different species present in the SEI: (a) ~282.7 eV for Na-C bond, corresponding to sodiated carbon (yellow), (b) ~284.8 eV for C–C or C-H bonds, corresponding to aliphatic chains and also hydrocarbon surface contamination (pink), (c) ~286.3–286.5 eV for C–O–C bonds (green), (d) ~288.6–288.7 eV for O=C–OR environments (cyan), and (e) ~289.8-290 eV for carbonate (–CO₃) environments (red). For MP:ClO₄⁻:PC:FEC, an additional peak was observed at ~290.7 eV corresponding to the C-F bond (blue) from the decomposition of the PVDF binder. Comparison of C 1s spectra for all the cases shows that the relative intensity ratios of the C–C component is higher than C–O except for PF₆⁻:PC:FEC, where the C-O environment dominates.

O 1s shows four representative peaks corresponding to : (i) ~531.6-531.9 eV for Na-O or Na-OH bonds (light pink), (ii) ~533.3-533.5 eV for O=C-OR or -CO₃ environment (light green), (iii) ~534.1-534.7 eV for C-O bonds (purple), and (iv) ~536.5-536.8 for Na-auger. In MP:ClO₄⁻:PC:FEC case, an additional peak corresponding to SnO₂ was observed, indicating the formation of a thinner SEI layer.

F 1s spectra display the signature of the P-F(green, at ~ 687.5 eV) and Na-F (red, at ~684.2 eV) ensuing from the degradation of NaPF₆ salts for MP:PF₆⁻:PC, and MP:PF₆⁻:PC:FEC. An intensity difference between Na-F and P-F peaks is clear for the PF₆-based electrolyte with and without FEC. Without FEC, the P-F peak dominates, and it's about 3.2 times higher than Na-F, indicating the insufficient formation of NaF. Salts with fluorine would be preferentially disintegrated prior to the PVDF binder, leading to the peak related to P-F in the case of MP:PF₆⁻:PC. However, the amount of Na-F is about 1.25 times greater than P-F after cycling with

FEC additive, where FEC is decomposed, preferably leading to the formation of Na-F. For MP:ClO₄⁻:PC: FEC, the P-F peak was absent; instead, a C-F peak from the defluorination of PVDF and a Na-F peak from the decomposition of FEC/PVDF was observed. In the fluorine-free electrolyte (MP:ClO₄⁻:PC), only a small peak of Na-F was observed, which suggests the reaction of Na with the only source of fluorine, PVDF. An intensive peak corresponding to C-F or P-F was not observed for the MP:ClO₄⁻:PC case indicating the formation of a thicker SEI layer (as observed from CV data analysis), where PVDF or PVDF degraded product was not exposed to the surface.

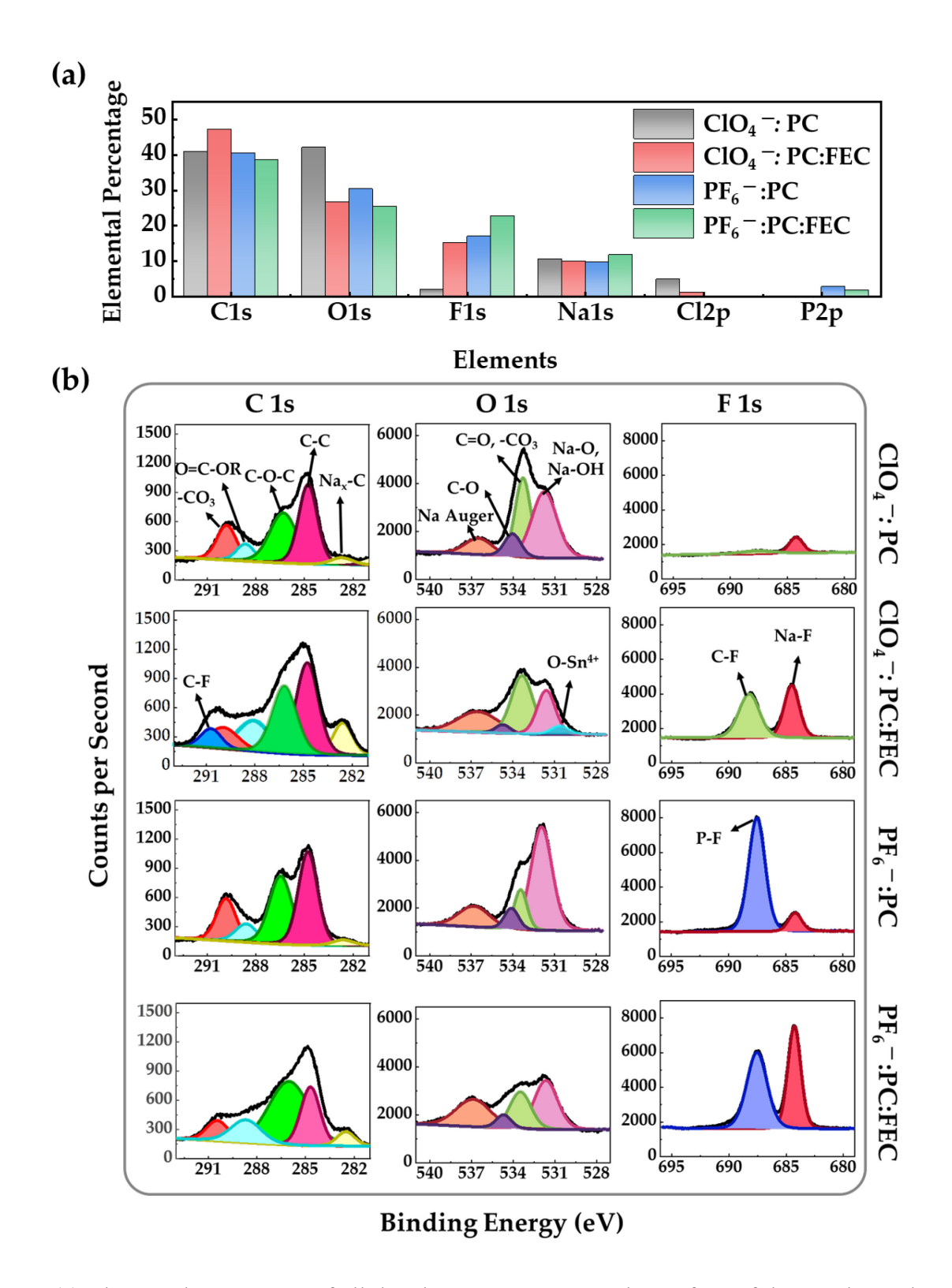


Figure 4. (a) Elemental percentage of all the elements present on the surface of the Sn electrode. (b) XPS core spectra comparison for microparticle (MP) based Sn electrodes. The Sn electrodes are taken from the cell after 10 cycles at 0.1 c-rate in different electrolytes.

Structural Evolution using XRD

Reference XRD spectra of ICDD Tin (β Sn:03-065-7657) were used to compare with the cycled electrodes for both NP and MP electrodes. The reflections for reference and cycled electrodes match with the Sn spectra in the database, as shown in **Figure 5(a)**. Moreover, the cycling curves show the key phase transitions that occur during sodiation and desodiation, i.e., Na_xSn voltage plateaus, but subtle changes in the crystal structure and the formation of side phases are not appreciable in the cycling data.²⁷

Figure 5(a)- (b) shows the comparison of all samples with the PC and PC: FEC electrolyte additive. An additional reflection is visible in the wavelength range of 4.5 Å to 5Å, which is not visible in the pristine or PC electrolyte samples. For Sn electrodes that are cycled with the FEC additive, it is observed that due to the electrochemical decomposition, there is a formation of NaF.^{28–30} The appearance of NaF is primarily observed in the electrolyte with FEC (Figure 5b), which is mostly due to the decomposition of fluorine-based electrolyte salts or the FEC solvent.^{31–33} However, research from Xu *et al.* proposed that the generated NaF reflection could be from the hydrolysis product due to trace moisture in the electrolyte solvents.^{34,35} If the salt anion is susceptible to hydrolysis, the generated HF reacts with the surface species and creates NaF, which can be visible in the solid electrolyte interphase.

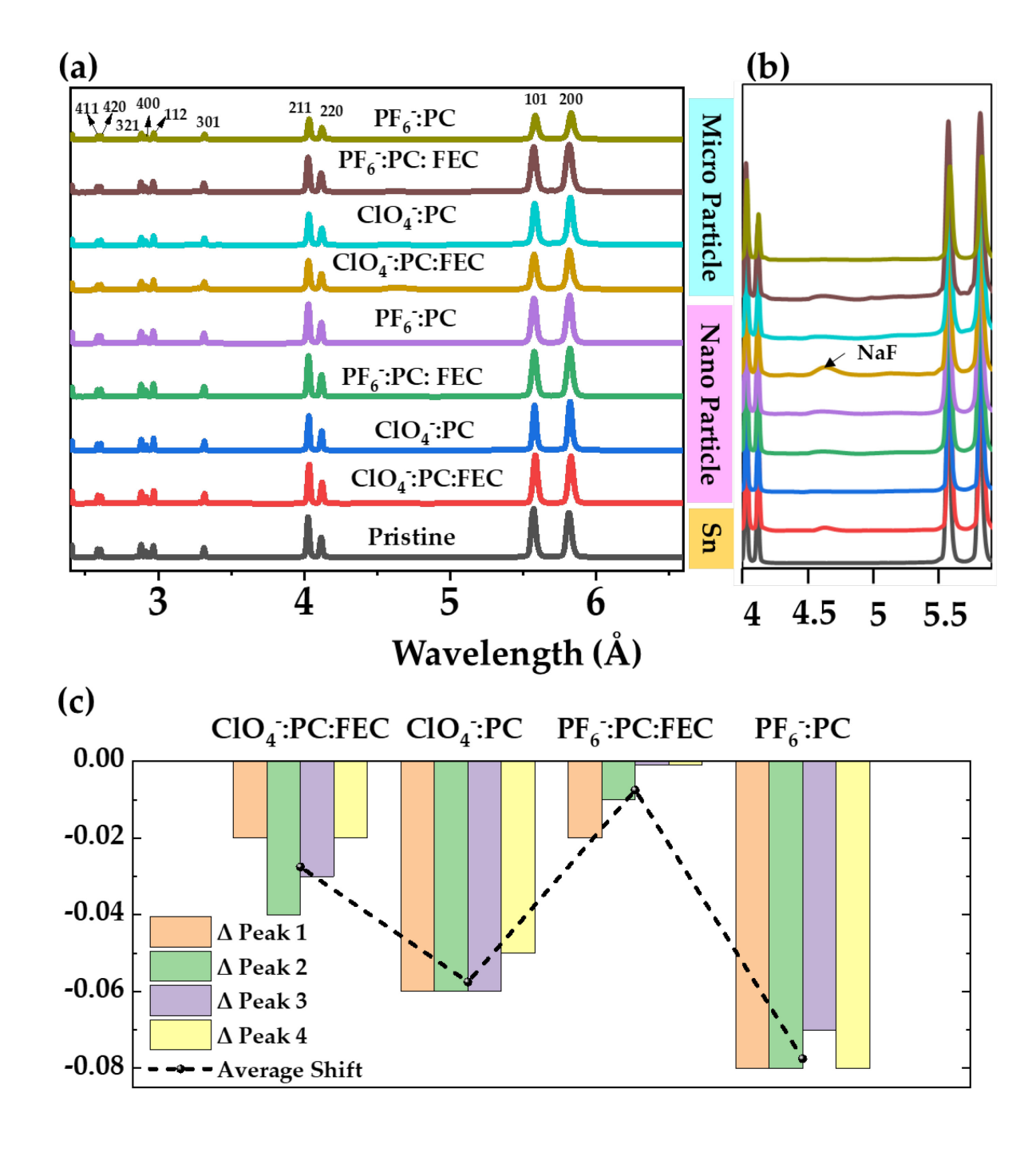


Figure 5. (a) Electrochemical side phases present on MP and NP cycled electrodes, (b) zoomedin image reveals the presence of NaF side phase in samples containing FEC. (c) Comparison of the first four reflection positions (at 5.81Å, 5.57Å, 4.12Å and 4.03Å) of all cycled NP electrodes vs. reference, showing the shift in reflections from the XRD data. Reflection numbering is from highest wavelength to lowest wavelength.

Table 1. Lattice parameters for cycled samples all have positive values, relating expansion of crystal structure with the shift in reflections to lower wavelengths.

Cycled Electrodes	Δa (Å)	Δb (Å)	Δc (Å)
NP ClO ₄ ⁻ :PC:FEC	0.0024	0.0024	0.0015
NP ClO ₄ ⁻ :PC	0.0092	0.0092	0.0059
NP PF ₆ ⁻ :PC:FEC	0.0033	0.0033	0.0024
NP PF ₆ ⁻ :PC	0.0073	0.0073	0.0042
MP ClO ₄ ⁻ :PC:FEC	0.0071	0.0071	0.0043
MP ClO ₄ ⁻ :PC	0.0086	0.0086	0.0054
MP PF ₆ ⁻ :PC:FEC	0.0071	0.0071	0.0043
MP PF ₆ ⁻ :PC	0.0027	0.0027	0.0022

Additionally, through XPS and EIS analysis, Vogt *et al.* show a correlation between the intensity of the NaF reflection and the FEC concentration.¹⁷ As the FEC concentration increases, the reflection intensity of NaF also increases due to the presence of additional fluorine. FEC-containing electrolytes tends to exhibit reduced reflection intensities of organic compounds, which is attributed to the fact that the organic surface films are suppressed by the decomposition of the FEC additive. This decomposition also helps to prevent PDVF from reacting with the electrolyte through cycling, therefore, decreasing the thermal decomposition of the sodiated Sn electrode with electrolyte and binder.²⁸ Based on these findings as well as congruent literature, we believe that

the additional reflection visible in the XRD spectra is NaF, produced by the degradation of the FEC additive in the electrolyte, which is also greater in microstructures with a higher surface area such as NP electrodes.

Moreover, the analysis of the reflection shift deviations was focused on the first four Sn reflections of each sample. The wavelength deviation was calculated by finding the difference between the reflection values of the reference and the samples. The deviation for each of the first four Sn reflections was averaged for each sample and presented as a method to correlate the change of the crystal structure among different electrolyte formulations. The reflection shifts for all cycled samples consistently drop to lower wavelengths (Figure 5c), which correlates directly to the expansion of the lattice parameters (Table 1). ^{36,37}

Specific focus on the NP electrodes due to their better capacity retention shows the most significant amount of reflection shifting, which occurred within electrolyte formulations without FEC. This is consistent with the appearance of a passivating layer for electrodes cycled with FEC. Figure 5(c) shows how NP ClO₄⁻:PC and PF₆⁻:PC had -0.0575 and -0.0775 shifts in wavelength, respectively, while their FEC-containing counterparts had -0.0275 and -0.0075 shifts, respectively. This effect can be attributed to volumetric expansion and change in length of crystal structure relating these changes to higher degradation on the electrode. Moreover, for electrodes with FEC, the appearance of the NaF side phase helps mitigate expansion and further degradation of the electrode particles, as well as limiting further degradation of the PVDF. Thus, the strong correspondence between the shift in XRD reflections and peak weakening in CV suggests that the irreversibility of the NP in the presence of PF₆⁻:PC electrolyte is strongly correlated with the crystallinity changes of intermediate phases.

Microstructural Characterization

To further understand the effects of electrode-electrolyte interface complexations occurring during sodiation/desodiation, the surface morphologies were observed in the pristine and cycled electrodes. **Figure 6** shows the SEM images of the surface morphology of the pristine MP (a, b) and NP (c, d) and aged electrodes (e-t). The surface of the MP shows more cracks than the NP Sn. NP Sn shows more agglomeration than MP due to higher surface energy caused by a higher surface area to volume ratio.

An evolving mesoscale structure impacting electrode performance is a critical behavior of Sn anodes in the Na-ion system. Expansion of Sn on sodiation alters the chemically active area, as well as its crystalline structure and reconfigures both the active material and supporting carbon/binder matrix. These changes alter the electrochemical performance. Particle size and electrolyte-dependent morphological changes of the aged electrodes (MP and NP) in ClO₄⁻:PC, ClO₄⁻:PC: FEC, PF₆⁻:PC, and PF₆⁻:PC: FEC electrolyte is shown in **Figure 6** and **S4-S7**. These changes from the post-mortem study include alteration of particle structure and fracture of the active material. SEM images revealed that the MP electrodes for all the electrolytes tested show much fewer cracks than pristine electrodes indicating the formation of a passivation layer. There is evidence of micropore formation in an MP electrode for all types of electrolytes. However, evidence of severe bulk electrode pulverization and cracking was observed for nano Sn with ClO₄⁻:PC electrolyte (Figures g-h). The higher resolution image for nano Sn shows the formation of a thin film wrapping the electrode particles. In ClO₄-:PC: FEC electrolyte, the NP electrode (Figures k-1) showed no evidence of polymeric film formation. Higher resolution images show isolated dark structures. Earlier investigation on decomposition mechanisms of electrolyte additives revealed that the SEI of FEC-based electrolyte poly(FEC) is only formed in small

quantities, independent of the FEC concentration, suggesting that FEC can be added to electrolytes as a co-solvent without worrying about dosage amount.³⁸ Also, FEC is a preferred additive for alloy-based material for which the SEI must be reformed in each cycle until all FEC is consumed and the cycling performance drops. Repetition of SEI layer formation and dissolution led to the formation of those island types of structural formations. The nano Sn with PF6-:PC based electrolyte (Figures o-p) also showed polymeric film formation similar to ClO₄⁻:PC. These polymeric film-wrapped Sn particles go through high volume expansion (around 420%) after full sodiation (Na₁₅Sn₄). In addition to substantial volume expansion, transport of ions during sodiation via the multi-phase diffusion process leads to a large concentration gradient induced load, which in turn results in significant mechanical degradation.^{39,40} During desodiation, the Sn particles experience high contraction. However, the stretches in the polymeric film during the sodiation process cause permanent deformation and show wrap type structures that form during the desodiation process. For PF₆⁻:PC: FEC-based electrolyte (Figure q-r), isolated structures were formed in the Sn MP electrodes. For nano Sn (Figures s-t), some additional structures were observed, which might be a different form of sodium stannite (Na₂SnO₃ or Na₄Sn₃O₈). When PVDF was the choice of binder, this type of structure was also found in PbTiO₃ electrodes where Pb species have recombined with Na and O and reprecipitated as micro-sized hexagonal particles.41

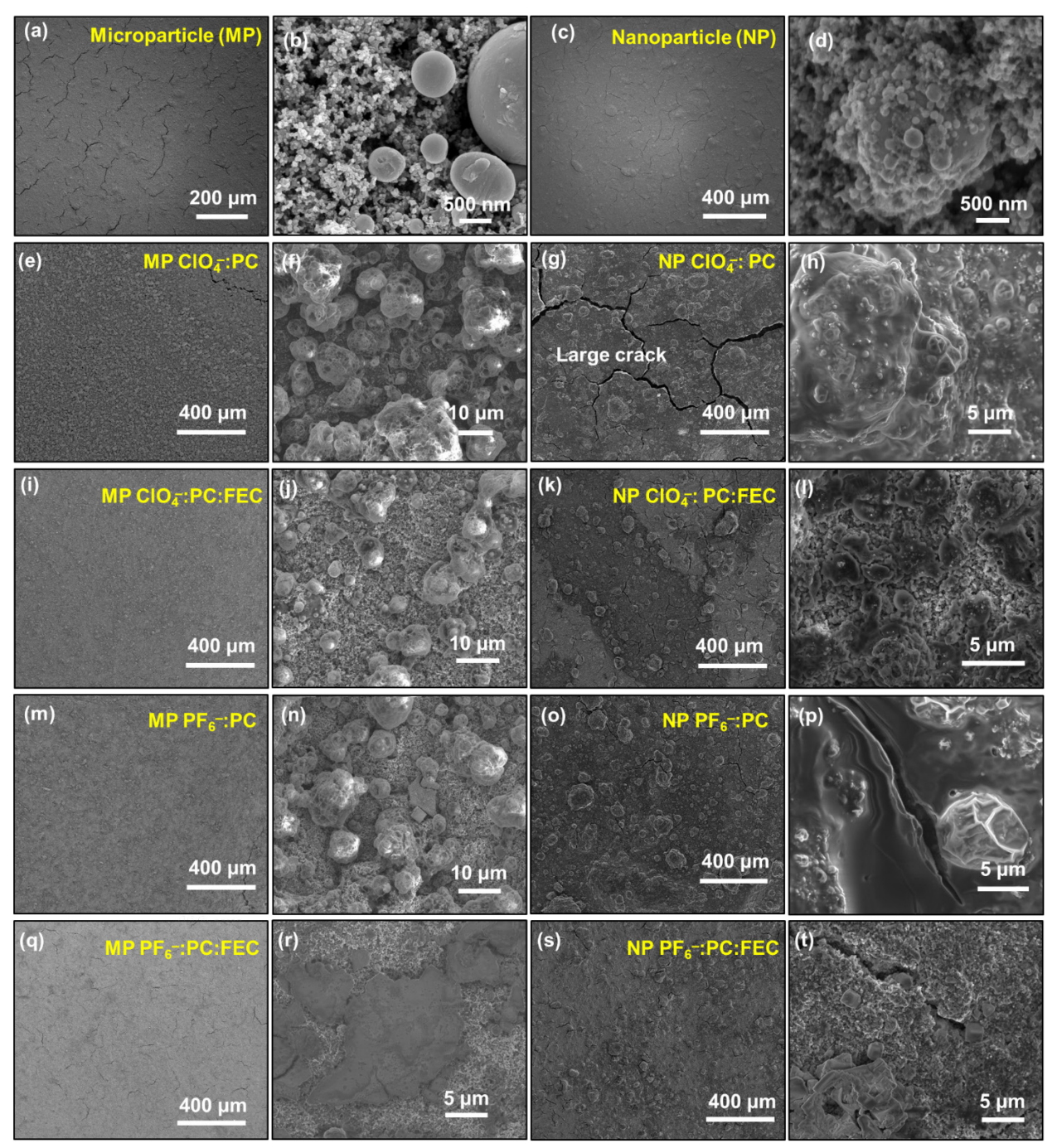


Figure 6. SEM images of the fresh electrode with PVDF at different magnifications. (a)-(b) Microparticle (MP) and (c)-(d) Nanoparticle-based electrode. SEM mages of aged electrodes with ClO_4^- :PC electrolyte (e)-(f) micro-Sn and (g)-(h) nano Sn, with ClO_4^- :PC: FEC electrolyte (i)-(j) micro-Sn and (k)-(l) nano Sn, with PF₆⁻:PC electrolyte (m)-(n) micro-Sn and (o)-(p) nano Sn, and with PF₆⁻:PC: FEC electrolyte (q)-(r) micro-Sn and (s)-(t) nano Sn at different magnifications. The cells were cycled at C/10 for 10 cycles.

3D Morphological Evolution using X-ray Tomography

To better understand the coupling of microstructural changes and electrochemical signatures for the Sn active material, an X-ray microtomography (μ CT) study was performed with Sn as the working electrode in half-cells with Na metal as the counter electrode.

The projection images obtained were reconstructed using TomoPy and segmented using the image histogram as a guide. 42 A region containing the electrode, the copper current collector, and open void space was selected from the pristine sample image data. The histogram of an ROI was obtained for this region, and initial thresholds were set to separate the high attenuation metallic phases (Sn and Cu), the carbon-binder domain (CBD), and the open void space. Here, the CBD region includes the PVDF binder, carbon black conductive additive, and sub-resolution active material particles and pore regions. This region may also include sodiated Sn particles (Na_xSn). Figure S1 shows how after the selection of the ROI, gray values obtained from the image histogram were used as a reference for segmenting other samples. Following the initial segmentation, the threshold was adjusted to yield a ratio of Sn to CBD that was within 20% of the value expected based on the initial weight fractions of the electrode components. This variation was considered acceptable due to the expected presence of sub-resolution void and active material within the regions designated as CBD.¹⁸ In prior work, these segmentation procedures based on variation in the grayscale values had successfully separated the different electrode components from each other depending on their attenuation. 18,43-45 As shown in Figure S1, other cycled electrodes show similar grayscale values, which enables segmentation of the Sn active material from supporting phase regions.

The gray values determined from the segmentation procedure noted above were applied to three regions extracted from the pristine electrode image data as well as image data acquired for the electrode cycled in ClO_4 ⁻:PC: FEC. Each of these regions was ~ $20\times50\times500$ µm. Once the segmentation of the electrode regions was complete, the regions were further subdivided into sample regions $20\times50\times100$ µm to enable faster characterization. The phase sizes, connectivity, and tortuosity of these regions were characterized using the methods of Grew *et al.* ^{18,43–45}

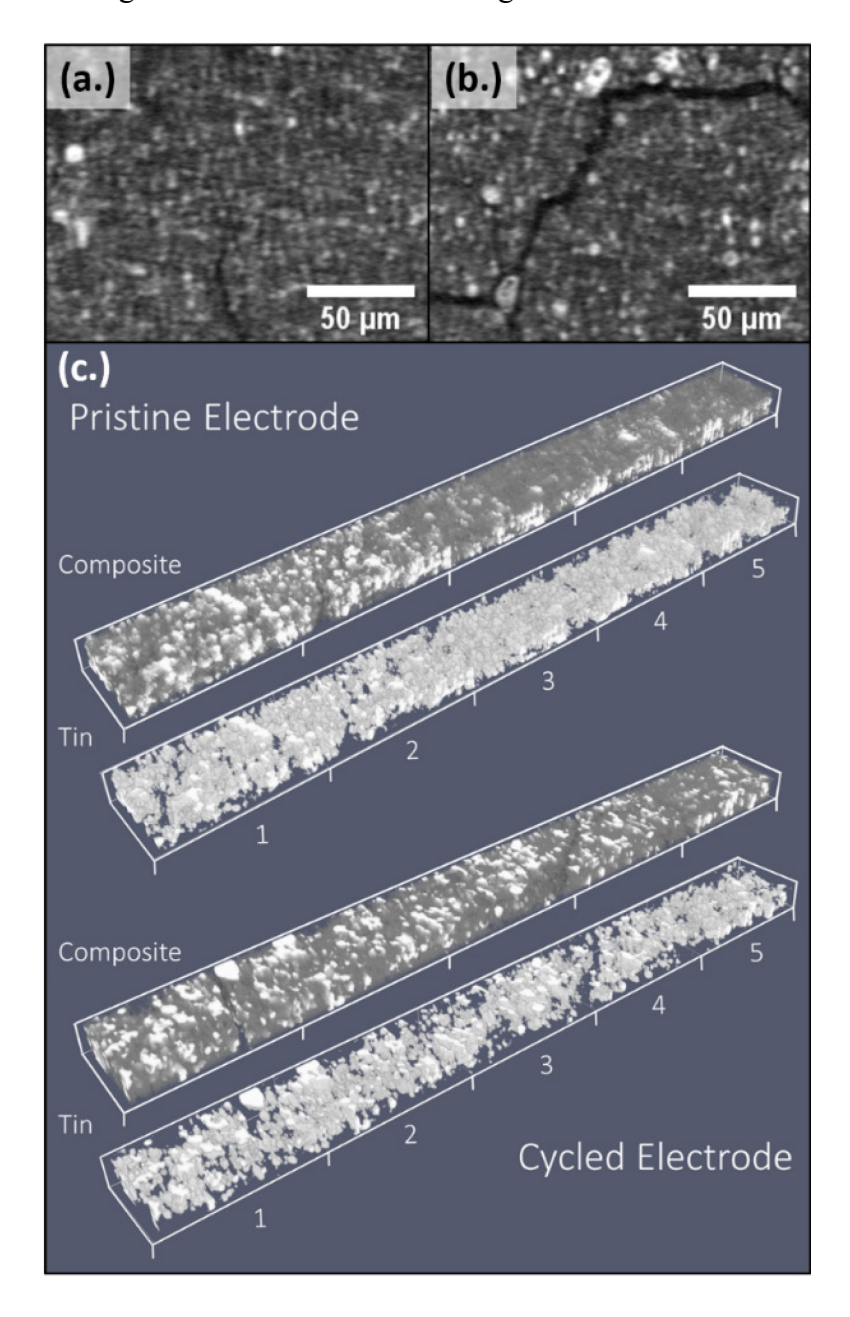


Figure 7. X-ray μ CT cross-sections from (a.) a pristine Sn composite electrode and (b.) an electrode cycled in ClO₄⁻:PC: FEC electrolyte. (c.) Renderings of the pristine and cycled electrodes showing the composite electrode and the Sn phase.

Figure 7 shows cross-sections of the μCT data (Figure 7a.) as well as three-dimensional renderings of the pristine and cycled electrodes (Figure 7b.). From this reconstruction, there is an apparent change in the quantity and size of Sn particles resulting from pulverization during cycling, as well as fractures in both the cross-sections and three-dimensional renderings. The decrease in size of Sn particles agrees with research conducted by Juarez-Robles *et al.* for the LIB system, which noted that increased counts of smaller particle sizes within an electrode represent the degradation of the active material by pulverization.

Phase size distributions and cumulative phase size distributions calculated using the methods of Grew et al. are shown in Figure 8 for the Sn, carbon-binder domain, and macropore regions within the electrode samples. These distributions provide quantitative observations that complement the visualization provided in Figure 7. **Figure 8(a-b)** represents the pristine electrode sample, while (c-d) represents the cycled electrode. Comparing the data from the pristine and the cycled electrode, clearly, the electrode cycling caused large diameter particles (15-20μm) breakdown; this decreased the overall particle size, which agrees with the visual reconstruction in Figure 7.

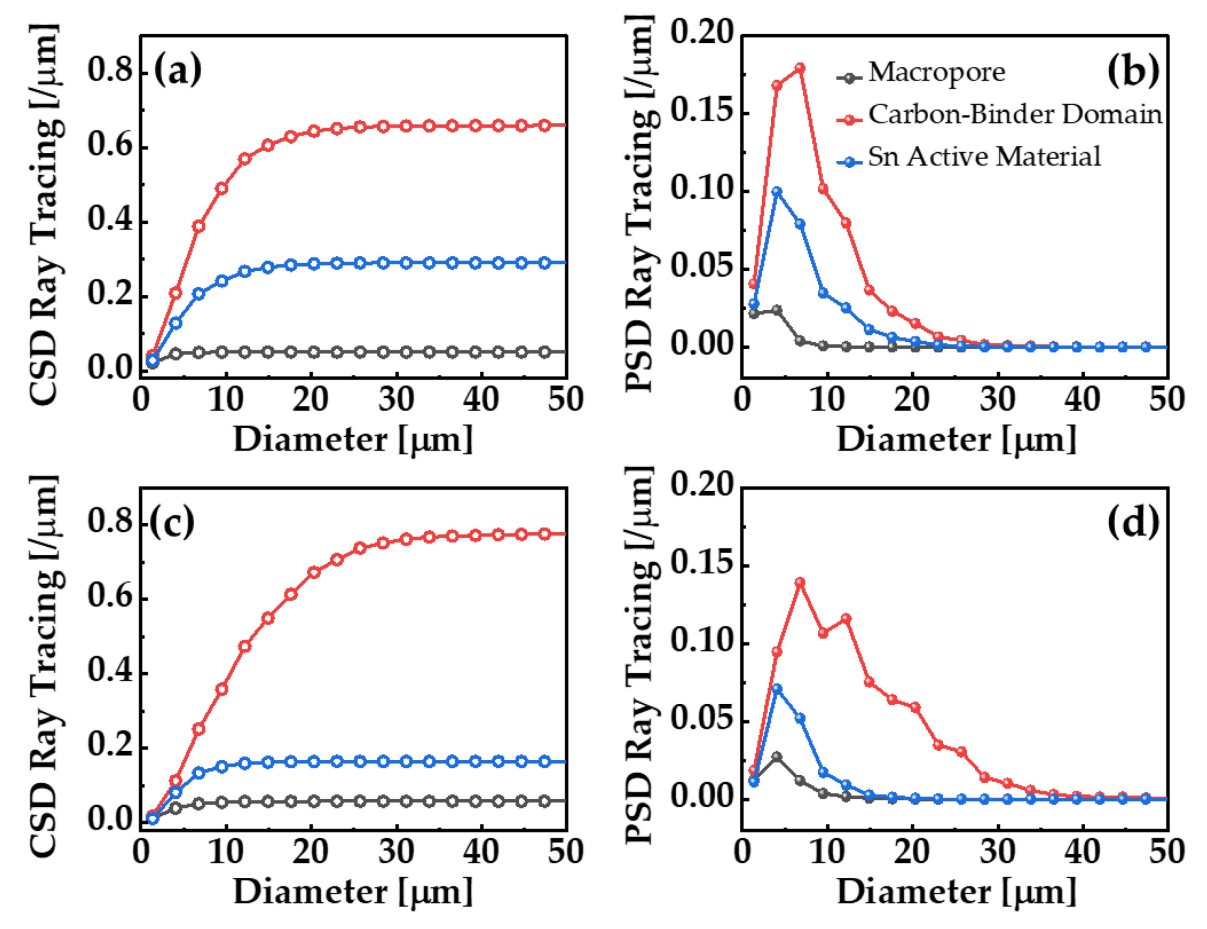


Figure 8. (a) Cumulative phase size distribution and (b) phase size distribution for pristine electrode and (c) cumulative phase size distribution and (d) phase size distribution for an electrode cycled in ClO₄⁻:PC: FEC electrolyte.

Additionally, pulverization of the Sn particles is observed based on two primary aspects of the collected data. The reduction of the volume fraction allocated to phase sizes with particles greater than 10µm and the growth of supporting CBD phase sizes. Moreover, there is a reduction in the Sn phase volume fraction below 10µm, which is expected from the material breaking down into sub-resolution sizes. Growth of the supporting phase sizes may be attributed to the addition of lower attenuating Na_xSn phases and the formation of sub-resolution Sn. Quantifying changes occurring at sub-micron resolutions would require a finer scale characterization method. Focusing on the macropore phase, the emergence of larger macropore regions in the cycled cell directly

results from the electrode fracture. The Sn pulverization also results in a breakdown of the network of connected active material, which is seen in the reduced connectivity and increased tortuosity of the Sn phase in Table 2.

Table 2. Tin and carbon/binder phase connectivity and tortuosity across the anode thickness for pristine and cycled anodes

Condition	Connectivity	Tortuosity
Pristine	0.9526	7.612
Cycled	0.6642	10.25
Pristine	0.9997	1.412
Cycled	0.9999	1.168
	Pristine Cycled Pristine	Cycled 0.6642 Pristine 0.9997

For comparison, only the connectivity and tortuosity in the y-direction (across the electrode thickness) are considered since it is the primary transport direction. The growth of the classified CBD regions, as shown in **Figures 8c-d**, results in reduced tortuosity. These results reflect prior observations for high-capacity materials where both the active material and supporting phases are altered by the cycling process. Active material changes are a direct result of the sodiation process, while the change in supporting phases results from the interaction between those phases with the expansion and contraction of the active material.

4. CONCLUSION

In this work, we have examined the sodiation-driven microstructure evolution of Sn-based alloy electrodes by correlating microstructural geometry changes, crystal structure, and electrochemical capacity degradation. It is evident that the changes in mesoscale morphology and chemical composition caused by sodiation in the presence of different electrolytes and different particle sizes yielded distinct contributions to the irreversible capacity of the Sn electrode. We found that for larger particles, the volumetric expansion and changes in the crystalline structure cause the reduction of the anode specific surface area available for electrochemical reaction and degenerate the mesoscale networks that support mass and charge transport leading to the limited cycle life of the Na-Sn system. Smaller particle sizes with larger surface area consumed a larger amount of Na from the inventory leading to lower coulombic efficiency; however, electrodes based on these smaller particles have higher capacity retention compared to the microparticles, especially in the additive-free electrolytes. For pure PC-based cells, the formation of a thicker passivation layer was evident from the weak CV signals and structures observed in the SEM images. The electrolyte additive FEC helped to reduce overpotentials after cycling with a stable SEI layer and enabled higher storage capacity retention for both micro and nanoparticles. The results in this work clearly indicate that the interface destabilization driven by electrolytes can be further compounded by binder-electrode microstructural interactions and can dominate the electrochemical signature of the electrode. These findings open a path for the manipulation of active material particle sizes and electrolyte additives for better sodium storage performance in the future.

ASSOCIATED CONTENT

Supporting Information

The additional data analysis, including X-ray image and histogram of the pristine electrode (Figure S1), charge-discharge capacity vs. cycle numbers of micro and nano Sn (Figure S2), and peak shift in XRD pattern for cycled Sn at different electrolyte combinations (Figure S3), are given. In addition to that, SEM images of aged micro and nano electrodes with NaClO₄:PC (Figure S4), NaClO₄:PC:FEC (Figure S5), NaPF₆:PC (Figure S6), NaPF₆:PC:FEC electrolytes (Figure S7) and FTIR spectra of Sn electrodes (Figure S8) are supplied.

AUTHOR INFORMATION

Corresponding Author

Partha P. Mukherjee - School of Mechanical Engineering, Purdue University, West Lafayette, Indiana 47907, United States, **ORCID:** 0000–0001–7900–7261, E-mail: pmukherjee@purdue.edu

Authors

- **Susmita Sarkar** School of Mechanical Engineering, Purdue University, West Lafayette, Indiana 47907, United States, **ORCID:** 0000-0001-9395-8549
- **Hernando J. Gonzalez Malabet** Department of Mechanical and Aerospace Engineering, The University of Alabama in Huntsville, Huntsville, Alabama 35899, United States, **ORCID:** 0000-0003-4287-362X
- **Megan Flannagin** Department of Mechanical and Aerospace Engineering, The University of Alabama in Huntsville, Huntsville, Alabama 35899, United States
- **Alex L'Antigua** Department of Mechanical and Aerospace Engineering, The University of Alabama in Huntsville, Huntsville, Alabama 35899, United States

Pavel D. Schevckenko – Advanced Photon Source, Argonne National Laboratory, Lemont, Illinois 60439, United States

George Nelson – Department of Mechanical and Aerospace Engineering, The University of Alabama in Huntsville, Huntsville, Alabama 35899, United States, **ORCID:** 0000-0002-1170-245X, E-mail: george.nelson@uah.edu

ACKNOWLEDGMENTS

Financial support from the National Science Foundation through a Collaborative Research Award (CBET-1804629 and CBET-1805656) is gratefully acknowledged. This research used resources of the Advanced Photon Source, a U.S. Department of Energy (DOE) Office of Science User Facility, operated for the DOE Office of Science by Argonne National Laboratory under Contract No. DE-AC02-06CH11357.

Notes

The authors declare no competing financial interest.

REFRENCES

- (1) Wang, L. P.; Yu, L.; Srinivasan, M.; Xu, Z. J.; Wang, X. Recent Developments in Electrode Materials for Sodium-Ion Batteries. *J. Mater. Chem. A* **2015**, *3* (18), 9353–9378. https://doi.org/10.1039/c4ta06467d.
- (2) Ma, C.; Xu, T.; Wang, Y. Advanced Carbon Nanostructures for Future High Performance Sodium Metal Anodes. *Energy Storage Mater.* **2020**, *25* (July 2019), 811–826. https://doi.org/10.1016/j.ensm.2019.09.007.
- (3) Hong, S. Y.; Kim, Y.; Park, Y.; Choi, A.; Choi, N. S.; Lee, K. T. Charge Carriers in Rechargeable Batteries: Na Ions vs. Li Ions. *Energy Environ. Sci.* **2013**, *6* (7), 2067–2081.

- https://doi.org/10.1039/c3ee40811f.
- (4) Kim, S. W.; Seo, D. H.; Ma, X.; Ceder, G.; Kang, K. Electrode Materials for Rechargeable Sodium-Ion Batteries: Potential Alternatives to Current Lithium-Ion Batteries. Adv. Energy Mater. 2012, 2 (7), 710–721. https://doi.org/10.1002/aenm.201200026.
- (5) Abraham, K. M. How Comparable Are Sodium-Ion Batteries to Lithium-Ion Counterparts? *ACS Energy Lett.* **2020**, *5* (11), 3544–3547. https://doi.org/10.1021/acsenergylett.0c02181.
- (6) Weeks, J. A.; Sun, H. H.; Srinivasan, H. S.; Burrow, J. N.; Guerrera, J. V.; Meyerson, M. L.; Dolocan, A.; Heller, A.; Mullins, C. B. Facile Synthesis of a Tin Oxide-Carbon Composite Lithium-Ion Battery Anode with High Capacity Retention. *ACS Appl. Energy Mater.* 2019, 2 (10), 7244–7255. https://doi.org/10.1021/acsaem.9b01205.
- (7) Baggetto, L.; Ganesh, P.; Meisner, R. P.; Unocic, R. R.; Jumas, J. C.; Bridges, C. A.; Veith, G. M. Characterization of Sodium Ion Electrochemical Reaction with Tin Anodes: Experiment and Theory. *J. Power Sources* **2013**, *234*, 48–59. https://doi.org/10.1016/j.jpowsour.2013.01.083.
- (8) Lin, Y. M.; Abel, P. R.; Gupta, A.; Goodenough, J. B.; Heller, A.; Mullins, C. B. Sn-Cu Nanocomposite Anodes for Rechargeable Sodium-Ion Batteries. ACS Appl. Mater. Interfaces 2013, 5 (17), 8273–8277. https://doi.org/10.1021/am4023994.
- (9) Wang, J. W.; Liu, X. H.; Mao, S. X.; Huang, J. Y. Microstructural Evolution of Tin Nanoparticles during in Situ Sodium Insertion and Extraction. *Nano Lett.* 2012, 12 (11), 5897–5902. https://doi.org/10.1021/nl303305c.
- (10) Górka, J.; Vix-Guterl, C.; Matei Ghimbeu, C. Recent Progress in Design of Biomass-

- Derived Hard Carbons for Sodium Ion Batteries. C 2016, 2 (4), 24. https://doi.org/10.3390/c2040024.
- (11) Liu, P.; Li, Y.; Hu, Y. S.; Li, H.; Chen, L.; Huang, X. A Waste Biomass Derived Hard Carbon as a High-Performance Anode Material for Sodium-Ion Batteries. *J. Mater. Chem. A* **2016**, *4* (34), 13046–13052. https://doi.org/10.1039/c6ta04877c.
- (12) Soto, F. A.; Yan, P.; Engelhard, M. H.; Marzouk, A.; Wang, C.; Xu, G.; Chen, Z.; Amine, K.; Liu, J.; Sprenkle, V. L.; El-Mellouhi, F.; Balbuena, P. B.; Li, X. Tuning the Solid Electrolyte Interphase for Selective Li- and Na-Ion Storage in Hard Carbon. *Adv. Mater.*2017, 29 (18). https://doi.org/10.1002/adma.201606860.
- (13) Forsyth, M.; Girard, G. M. A.; Basile, A.; Hilder, M.; MacFarlane, D. R.; Chen, F.; Howlett, P. C. Inorganic-Organic Ionic Liquid Electrolytes Enabling High Energy-Density Metal Electrodes for Energy Storage. *Electrochim. Acta* 2016, 220, 609–617. https://doi.org/10.1016/j.electacta.2016.10.134.
- (14) Yamamoto, T.; Nohira, T.; Hagiwara, R.; Fukunaga, A.; Sakai, S.; Nitta, K.; Inazawa, S. Improved Cyclability of Sn-Cu Film Electrode for Sodium Secondary Battery Using Inorganic Ionic Liquid Electrolyte. *Electrochim. Acta* 2014, *135*, 60–67. https://doi.org/10.1016/j.electacta.2014.04.159.
- (15) Kuo, L. Y.; Moradabadi, A.; Huang, H. F.; Hwang, B. J.; Kaghazchi, P. Structure and Ionic Conductivity of the Solid Electrolyte Interphase Layer on Tin Anodes in Na-Ion Batteries. *J. Power Sources* 2017, 341, 107–113. https://doi.org/10.1016/j.jpowsour.2016.11.077.
- (16) Ponrouch, A.; Marchante, E.; Courty, M.; Tarascon, J. M.; Palacín, M. R. In Search of an Optimized Electrolyte for Na-Ion Batteries. *Energy Environ. Sci.* **2012**, *5* (9), 8572–8583.

- https://doi.org/10.1039/c2ee22258b.
- (17) Vogt, L. O.; El Kazzi, M.; Jämstorp Berg, E.; Pérez Villar, S.; Novák, P.; Villevieille, C. Understanding the Interaction of the Carbonates and Binder in Na-Ion Batteries: A Combined Bulk and Surface Study. *Chem. Mater.* 2015, 27 (4), 1210–1216. https://doi.org/10.1021/cm5039649.
- (18) Rajendra, T.; Mistry, A. N.; Patel, P.; Ausderau, L. J.; Xiao, X.; Mukherjee, P. P.; Nelson, G. J. Quantifying Transport, Geometrical, and Morphological Parameters in Li-Ion Cathode Phases Using X-Ray Microtomography. ACS Appl. Mater. Interfaces 2019, 11 (22), 19933–19942. https://doi.org/10.1021/acsami.8b22758.
- (19) Pender, J. P.; Jha, G.; Youn, D. H.; Ziegler, J. M.; Andoni, I.; Choi, E. J.; Heller, A.; Dunn, B. S.; Weiss, P. S.; Penner, R. M.; Mullins, C. B. Electrode Degradation in Lithium-Ion Batteries. ACS Nano 2020, 14 (2), 1243–1295.
 https://doi.org/10.1021/acsnano.9b04365.
- (20) Liu, C.; Neale, Z. G.; Cao, G. Understanding Electrochemical Potentials of Cathode Materials in Rechargeable Batteries. *Mater. Today* 2016, 19 (2), 109–123. https://doi.org/10.1016/j.mattod.2015.10.009.
- (21) Ovejas, V. J.; Cuadras, A. Effects of Cycling on Lithium-Ion Battery Hysteresis and Overvoltage. *Sci. Rep.* **2019**, *9* (1), 1–9. https://doi.org/10.1038/s41598-019-51474-5.
- (22) Ovejas, V. J.; Cuadras, A. State of Charge Dependency of the Overvoltage Generated in Commercial Li-Ion Cells. *J. Power Sources* **2019**, *418* (January), 176–185. https://doi.org/10.1016/j.jpowsour.2019.02.046.
- (23) Zhu, G.; Wang, Y.; Yang, S.; Qu, Q.; Zheng, H. Correlation between the Physical Parameters and the Electrochemical Performance of a Silicon Anode in Lithium-Ion

- Batteries. J. Mater. **2019**, 5 (2), 164–175. https://doi.org/10.1016/j.jmat.2019.03.005.
- (24) Han, M.; Zhu, C.; Zhao, Q.; Chen, C.; Tao, Z.; Xie, W.; Cheng, F.; Chen, J. In Situ Atomic Force Microscopic Studies of Single Tin Nanoparticle: Sodiation and Desodiation in Liquid Electrolyte. ACS Appl. Mater. Interfaces 2017, 9 (34), 28620–28626. https://doi.org/10.1021/acsami.7b08870.
- (25) Xu, Y.; Zhu, Y.; Liu, Y.; Wang, C. Electrochemical Performance of Porous Carbon/Tin Composite Anodes for Sodium-Ion and Lithium-Ion Batteries. *Adv. Energy Mater.* **2013**, 3 (1), 128–133. https://doi.org/10.1002/aenm.201200346.
- (26) Wang, L.; Ni, Y.; Lei, K.; Dong, H.; Tian, S.; Li, F. 3D Porous Tin Created by Tuning the Redox Potential Acts as an Advanced Electrode for Sodium-Ion Batteries. *ChemSusChem* 2018, 11 (19), 3376–3381. https://doi.org/10.1002/cssc.201801662.
- Zhang, B.; Rousse, G.; Foix, D.; Dugas, R.; Corte, D. A. D.; Tarascon, J. M. Microsized Sn as Advanced Anodes in Glyme-Based Electrolyte for Na-Ion Batteries. *Adv. Mater.*2016, 28 (44), 9824–9830. https://doi.org/10.1002/adma.201603212.
- (28) Lee, Y.; Lim, H.; Kim, S. O.; Kim, H. S.; Kim, K. J.; Lee, K. Y.; Choi, W. Thermal Stability of Sn Anode Material with Non-Aqueous Electrolytes in Sodium-Ion Batteries. *J. Mater. Chem. A* **2018**, *6* (41), 20383–20392. https://doi.org/10.1039/c8ta07854h.
- (29) Wiemers-Meyer, S.; Winter, M.; Nowak, S. Mechanistic Insights into Lithium Ion Battery Electrolyte Degradation-a Quantitative NMR Study. *Phys. Chem. Chem. Phys.* **2016**, *18* (38), 26595–26601. https://doi.org/10.1039/c6cp05276b.
- (30) Fondard, J.; Irisarri, E.; Courrèges, C.; Palacin, M. R.; Ponrouch, A.; Dedryvère, R. SEI Composition on Hard Carbon in Na-Ion Batteries After Long Cycling: Influence of Salts (NaPF 6, NaTFSI) and Additives (FEC, DMCF). J. Electrochem. Soc. 2020, 167 (7),

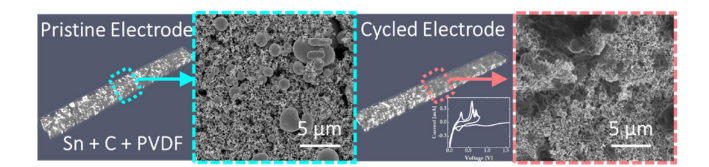
- 070526. https://doi.org/10.1149/1945-7111/ab75fd.
- (31) Jang, J. Y.; Lee, Y.; Kim, Y.; Lee, J.; Lee, S. M.; Lee, K. T.; Choi, N. S. Interfacial Architectures Based on a Binary Additive Combination for High-Performance Sn4P3 Anodes in Sodium-Ion Batteries. *J. Mater. Chem. A* **2015**, *3* (16), 8332–8338. https://doi.org/10.1039/c5ta00724k.
- (32) Profatilova, I. A.; Kim, S. S.; Choi, N. S. Enhanced Thermal Properties of the Solid Electrolyte Interphase Formed on Graphite in an Electrolyte with Fluoroethylene Carbonate. *Electrochim. Acta* 2009, 54 (19), 4445–4450.
 https://doi.org/10.1016/j.electacta.2009.03.032.
- (33) El Ouatani, L.; Dedryvère, R.; Siret, C.; Biensan, P.; Reynaud, S.; Iratçabal, P.; Gonbeau, D. The Effect of Vinylene Carbonate Additive on Surface Film Formation on Both Electrodes in Li-Ion Batteries. *J. Electrochem. Soc.* 2009, 156 (2), A103. https://doi.org/10.1149/1.3029674.
- (34) Xu, G. L.; Amine, R.; Abouimrane, A.; Che, H.; Dahbi, M.; Ma, Z. F.; Saadoune, I.; Alami, J.; Mattis, W. L.; Pan, F.; Chen, Z.; Amine, K. Challenges in Developing Electrodes, Electrolytes, and Diagnostics Tools to Understand and Advance Sodium-Ion Batteries. Adv. Energy Mater. 2018, 8 (14), 1–63. https://doi.org/10.1002/aenm.201702403.
- (35) Xu, K. Nonaqueous Liquid Electrolytes for Lithium-Based Rechargeable Batteries. *Chem. Rev.* **2004**, *104* (10), 4303–4417. https://doi.org/10.1021/cr030203g.
- (36) Huang, Y.; Zhao, L.; Li, L.; Xie, M.; Wu, F.; Chen, R. Electrolytes and Electrolyte/Electrode Interfaces in Sodium-Ion Batteries: From Scientific Research to Practical Application. *Adv. Mater.* **2019**, *31* (21), 1–41.

- https://doi.org/10.1002/adma.201808393.
- (37) Ma, L.; Cui, J.; Yao, S.; Liu, X.; Luo, Y.; Shen, X.; Kim, J. K. Dendrite-Free Lithium Metal and Sodium Metal Batteries. *Energy Storage Mater.* **2020**, *27* (November 2019), 522–554. https://doi.org/10.1016/j.ensm.2019.12.014.
- (38) Schwenke, K. U.; Solchenbach, S.; Demeaux, J.; Lucht, B. L.; Gasteiger, H. A. The Impact of CO 2 Evolved from VC and FEC during Formation of Graphite Anodes in Lithium-Ion Batteries . J. Electrochem. Soc. 2019, 166 (10), A2035–A2047. https://doi.org/10.1149/2.0821910jes.
- (39) Barai, P.; Huang, B.; Dillon, S. J.; Mukherjee, P. P. Mechano-Electrochemical Interaction Gives Rise to Strain Relaxation in Sn Electrodes. *J. Electrochem. Soc.* **2016**, *163* (14), A3022–A3035. https://doi.org/10.1149/2.0801614jes.
- (40) Barai, P.; Mukherjee, P. P. Mechano-Electrochemical Stochastics in High-Capacity Electrodes for Energy Storage. *J. Electrochem. Soc.* **2016**, *163* (6), A1120–A1137. https://doi.org/10.1149/2.01191606jes.
- (41) Zhang, Y.; Ji, M.; Liu, Z.; He, Y.; Hu, Y.; Yang, Q.; Li, B.; Wang, J. Electrochemical Properties of PX-Phase PbTiO3 Electrode for Sodium Ion Batteries. RSC Adv. 2017, 7 (41), 25678–25684. https://doi.org/10.1039/c7ra03622a.
- (42) Gürsoy, D.; De Carlo, F.; Xiao, X.; Jacobsen, C. TomoPy: A Framework for the Analysis of Synchrotron Tomographic Data. *J. Synchrotron Radiat.* **2014**, *21* (5), 1188–1193. https://doi.org/10.1107/S1600577514013939.
- (43) Gonzalez Malabet, H. J.; Juarez Robles, D.; de Andrade, V.; Mukherjee, P. P.; Nelson, G. J. In Operando XANES Imaging of High Capacity Intermetallic Anodes for Lithium Ion Batteries. J. Electrochem. Soc. 2020, 167 (4), 040523. https://doi.org/10.1149/1945-

7111/ab78fb.

- (44) Juarez-Robles, D.; Gonzalez-Malabet, H. J.; L'Antigua, M.; Xiao, X.; Nelson, G. J.;
 Mukherjee, P. P. Elucidating Lithium Alloying-Induced Degradation Evolution in HighCapacity Electrodes. ACS Appl. Mater. Interfaces 2019, 11 (1), 563–577.
 https://doi.org/10.1021/acsami.8b14242.
- (45) Trembacki, B. L.; Mistry, A. N.; Noble, D. R.; Ferraro, M. E.; Mukherjee, P. P.; Roberts, S. A. Editors' Choice—Mesoscale Analysis of Conductive Binder Domain Morphology in Lithium-Ion Battery Electrodes. *J. Electrochem. Soc.* 2018, 165 (13), E725–E736. https://doi.org/10.1149/2.0981813jes.

Table of Contents (TOC)/Abstract Graphic



Supporting Information

Multiscale Electro-Chemo-Mechanics Interaction and Degradation Analytics of Sn Electrodes

for Sodium-ion Batteries

Susmita Sarkar¹, Hernando J. Gonzalez-Malabet², Megan Flannagin², Alex L'Antigua², Pavel D. Shevchenko ³, and George J. Nelson^{2,*}, and Partha P. Mukherjee^{1,*}

^{*}Correspondence: george.nelson@uah.edu (G. J. Nelson); pmukherjee@purdue.edu (P. P. Mukherjee)

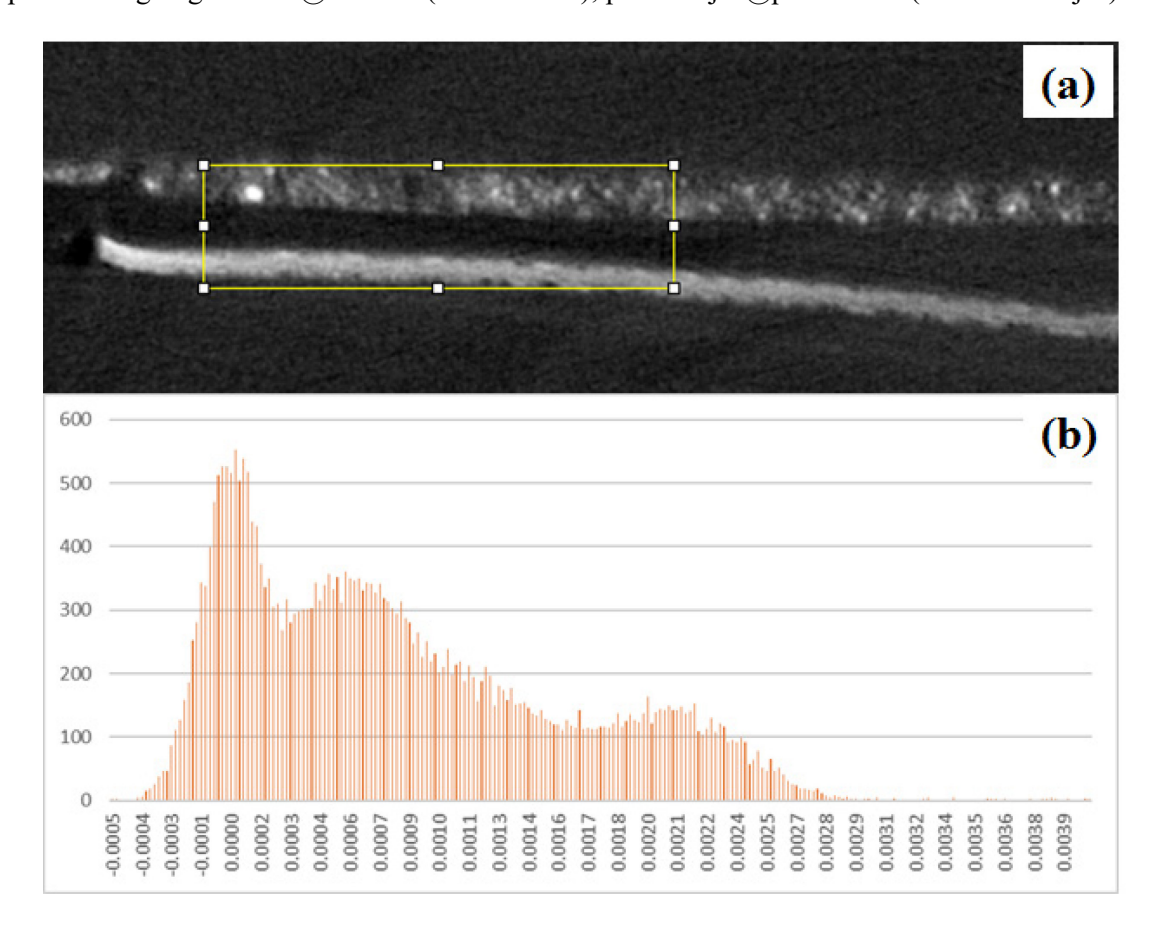


Figure S1. X-ray images were obtained from the Pristine electrode. (a) region of interest is selected in the yellow box, (b) gray value histogram of the selected region of interest (ROI). Gray values of ROI are used to compare with cycled electrodes.

¹School of Mechanical Engineering, Purdue University, West Lafayette, Indiana 47907, United States

²Department of Mechanical and Aerospace Engineering, The University of Alabama in Huntsville, Huntsville, Alabama 35899, United States

³Advanced Photon Source, Argonne National Laboratory, Lemont, Illinois 60439, United States

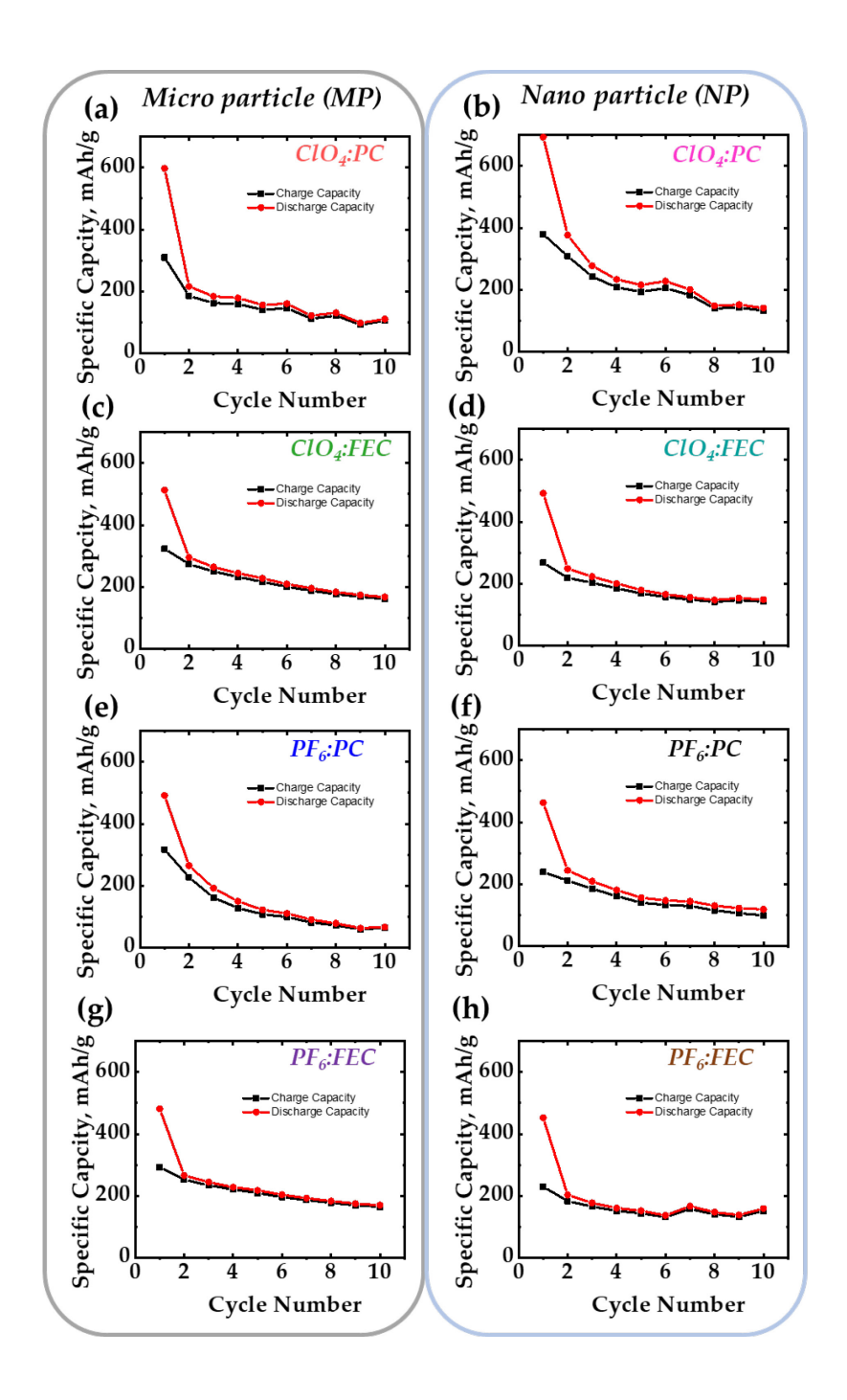


Figure S2. Charge-discharge capacity vs. cycle numbers of Sn microparticle (MP) and nanoparticle (NP) in different electrolytes: (a) MP: ClO₄⁻: PC, (b) NP: ClO₄⁻: PC, (c) MP: ClO₄⁻ PC: FEC, (d) NP: ClO₄⁻ PC: FEC, (e) MP: PF₆⁻: PC, (f) NP: PF₆⁻: PC, (g) MP: PF₆⁻: PC: FEC, and (h) NP: PF₆⁻: PC: FEC. The cells are cycled at 0.1 c-rate.

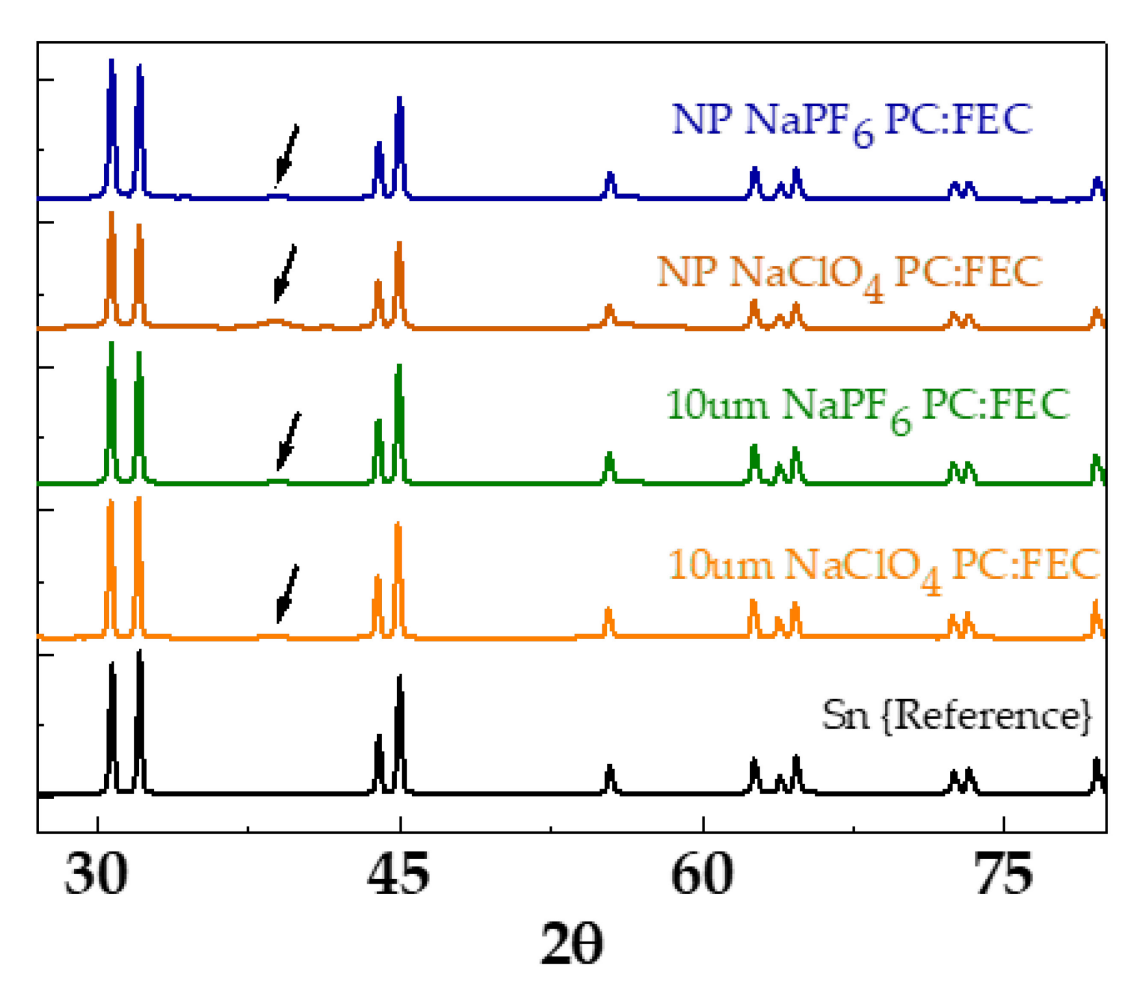


Figure S3. Cycled Sn electrodes peak shift and average comparisons for the different electrolyte combinations.

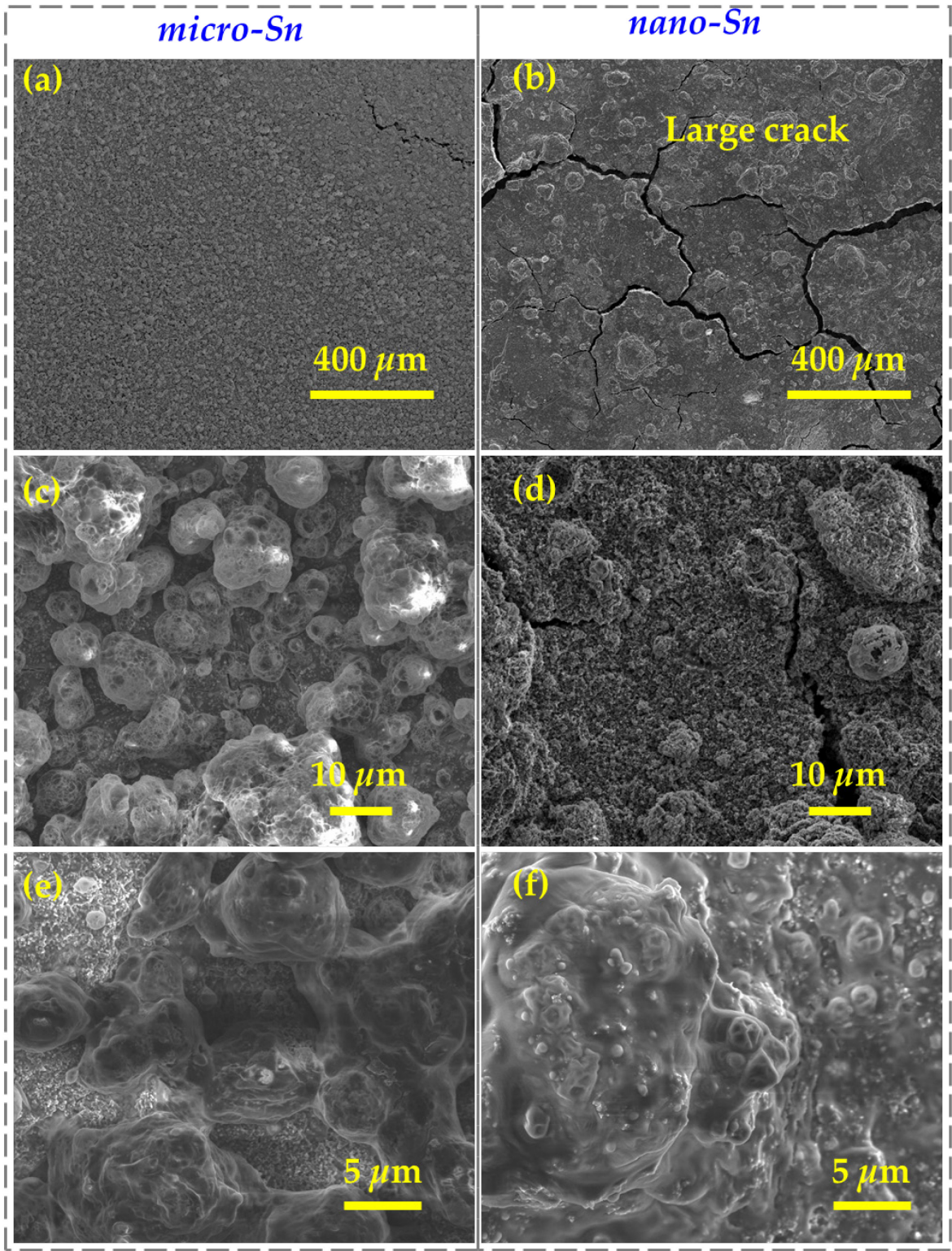


Figure S4. SEM images of the aged electrodes with NaClO₄:PC electrolyte at different magnifications (a),(c),(e) micro-Sn and (b),(d),(f) nano Sn. The cells were cycled at c/10 for 10 cycles.

NaClO₄:PC:FEC

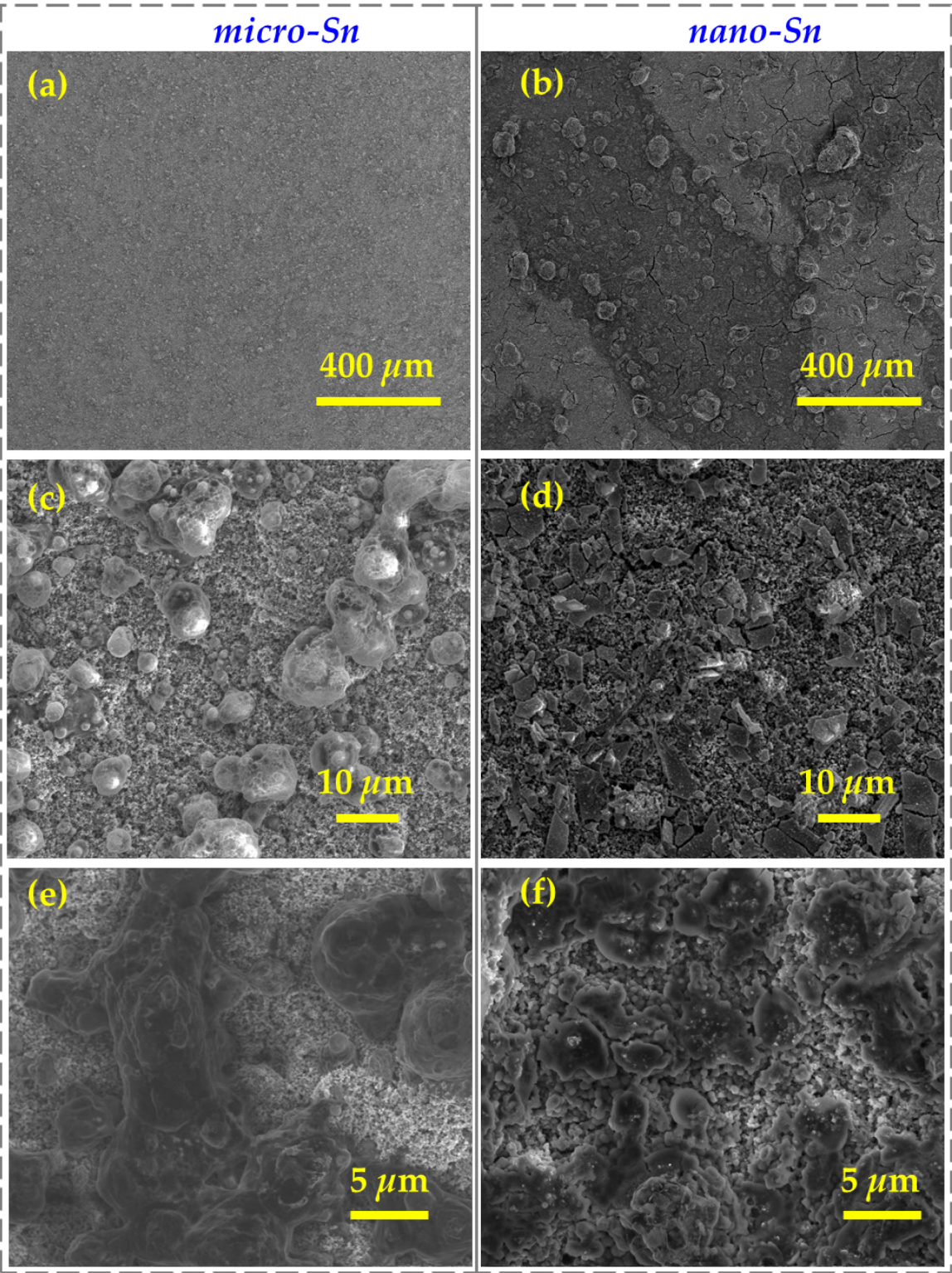


Figure S5. SEM images of the aged electrodes with NaClO₄:PC:FEC electrolyte at different magnifications (a),(c),(e) micro-Sn and (b),(d),(f) nano Sn. The cells were cycled at c/10 for 10 cycles.





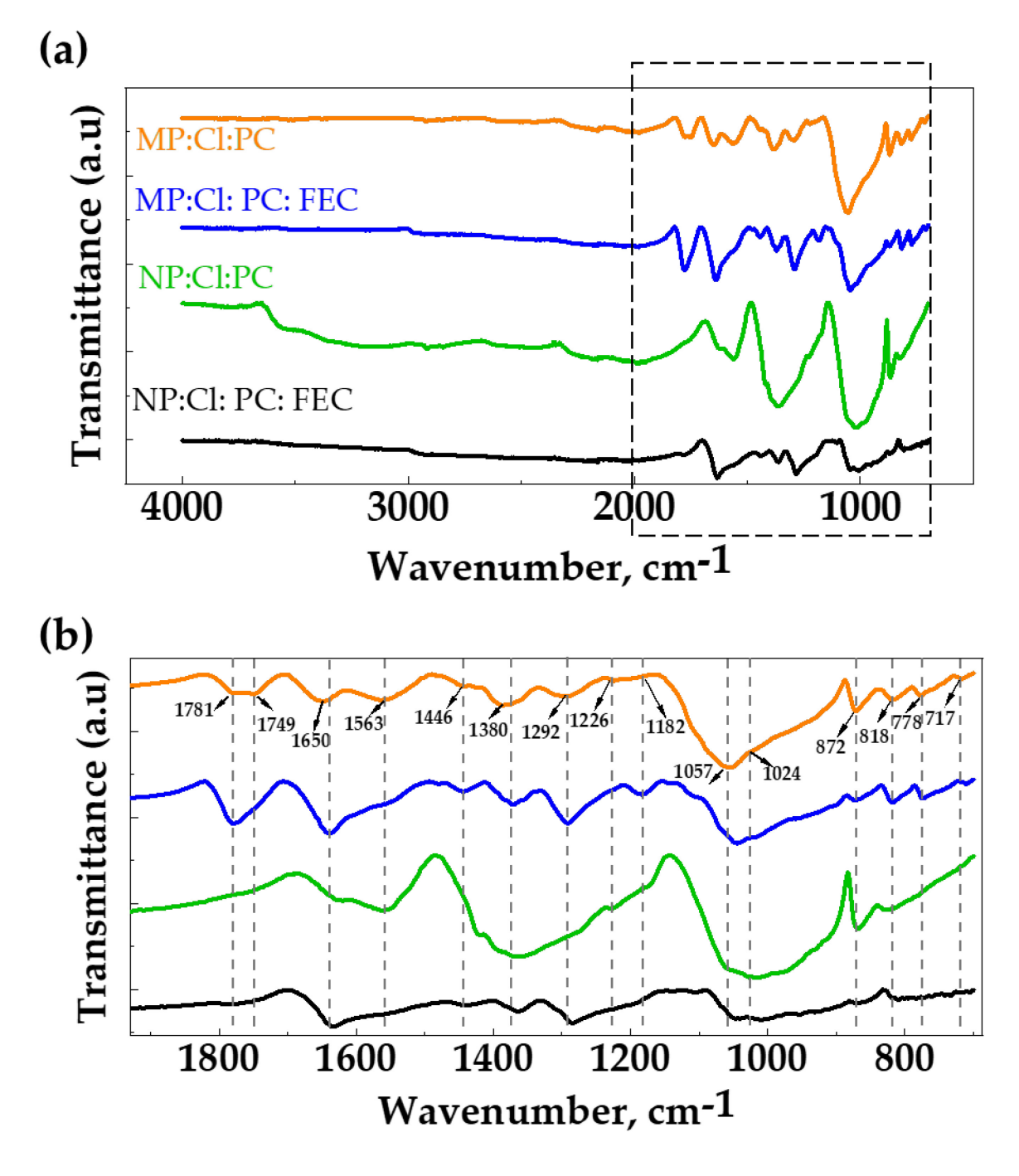


Figure S8. (a) FTIR core spectra comparison for microparticle (MP) and nanoparticle (NP) based Sn electrodes. (b) zoomed-in segment of rectangular selection of plot (a). The Sn electrodes are taken from the cell after 1 cycle at 0.1 C-rate in different electrolytes.